



Plasmonic resonances of slender nanometallic rings

Matias Ruiz

School of Mathematics, University of Edinburgh, Edinburgh EH9 3FD, United Kingdom

Ory Schnitzer 

Department of Mathematics, Imperial College London, London SW7 2AZ, United Kingdom

 (Received 4 July 2021; revised 23 February 2022; accepted 28 February 2022; published 14 March 2022)

We develop an approximate quasistatic theory describing the low-frequency plasmonic resonances of slender nanometallic rings and configurations thereof. First, we use asymptotic arguments to reduce the plasmonic eigenvalue problem governing the geometric (material- and frequency-independent) modes of a given ring structure to a one-dimensional periodic integrodifferential problem in which the eigenfunctions are represented by azimuthal voltage and polarization-charge profiles associated with each ring. Second, we obtain closed-form solutions to the reduced eigenvalue problem for azimuthally invariant rings (including torus-shaped rings but also allowing for noncircular cross-sectional shapes), as well as coaxial dimers and chains of such rings. For more general geometries, involving azimuthally nonuniform rings and noncoaxial structures, we solve the reduced eigenvalue problem using a semianalytical scheme based on Fourier expansions of the reduced eigenfunctions. Third, we used the asymptotically approximated modes, in conjunction with the quasistatic spectral theory of plasmonic resonance, to study and interpret the frequency response of a wide range of nanometallic slender-ring structures under plane-wave illumination.

DOI: [10.1103/PhysRevB.105.125412](https://doi.org/10.1103/PhysRevB.105.125412)

I. INTRODUCTION

Localized-surface-plasmon resonance, namely, the excitation of collective electric-field and electron-charge-density oscillations in metallic nanoparticles and nanostructures, has been instrumental over the past several decades in enabling new techniques for manipulating visible and near-infrared electromagnetic waves on nanometric scales, with applications including sensing, targeted heating, and metamaterials [1,2]. An important motif in fundamental research as well as applications has been the use of nearly singular, i.e., multiple-scale, geometries to achieve tunable and high-quality resonances, field enhancement in nanoscale “hotspots,” and for probing light-matter interactions and nonclassical phenomena [3–7].

The class of multiple-scale nanometallic structures most extensively studied in nanoplasmonics consists of closely spaced particles and similarly particles very near to a metallic substrate [8–22]. Such structures exhibit a rich spectrum comprised of several distinct families of modes characterized by their symmetries, as well as behavior in the limit where the aspect ratio κ , say the ratio of particle radius to gap width, is large. Particular emphasis has been given to bonding-gap modes, which are characterized by localization of the electric field to the gap, with the field directed across the gap. For large κ , the characteristic angular frequencies ω associated with these modes behave roughly like $\omega/\omega_p \simeq 1/\kappa^{1/4}$, wherein ω_p denotes the plasma angular frequency [17]. For large κ , the first few bonding-gap modes strongly couple with incident radiation, giving rise to low-frequency resonances associated with a giant field enhancement in the gap.

Another class of multiple-scale nanometallic structures that is commonly employed consists of slender particles such as high-aspect-ratio nanorods and spheroids [23–30]. Parallels can be drawn between the bonding-gap modes of closely spaced particles and the longitudinal modes of slender particles, which are characterized by polarization-charge distributions that for sufficient slenderness vary mainly along the particle axis. The latter longitudinal modes redshift as the particle becomes more and more slender, analogously to the redshift of the bonding-gap modes described above. In the slender-particle case, however, the plasmon-frequency redshift is far more singular: $\omega/\omega_p \simeq 1/\kappa$, where now κ represents the ratio of length to thickness [25]. Accordingly, the first few longitudinal modes of a slender particle typically give rise to remarkably low-frequency plasmonic resonances (down to the near-infrared regime), which are typically associated with high-quality factors and distinctive directional characteristics.

In comparison with straight slender particles, curved slender particles such as slender rings and helices are more subwavelength at their longitudinal resonances. Indeed, let the length and thickness of some slender particle be $2l$ and $2b$, respectively; the scaling $\omega/\omega_p \simeq 1/\kappa$ implies longitudinal resonances at wavelengths λ roughly proportional to $(l/b)\lambda_p$, where $\lambda_p = 2\pi c/\omega_p$ and c is the speed of light in vacuum. Hence, if the characteristic linear dimension of the particle is $2a$, we have that $a/\lambda \simeq (a/l)(b/\lambda_p)$. One avenue to reducing the latter size factor is to reduce b , though this is ultimately limited by manufacturing capabilities as well as nonclassical effects at subnanometric scales. An alternative avenue is to coil the centerline so as to decrease a/l . In particular, a/l is unity for a straight particle and $1/\pi$ for a circular ring.

The above characteristics of high-aspect-ratio nanometallic particles can be indirectly inferred from classical analytical solutions for cylinder and sphere dimers, ellipsoids, and tori, which are exact in the quasistatic approximation [2,31–37]. While these solutions allow for arbitrary aspect ratio, they are limited to separable geometries. Even then, exact solutions tend to be cumbersome and sometimes it is not straightforward to extract singular behaviors in the high-aspect-ratio limit. For more general geometries, analytical solutions are unavailable, whereas brute-force finite-element simulations become expensive at high aspect ratios. An alternative, more insightful and versatile, theoretical approach is to consider the high-aspect-ratio limit, in which plasmonic resonance is expected to be most pronounced, from the outset, using tools of asymptotic analysis and singular-perturbation theory [38]. The latter tools are classical, though their application to plasmonics is relatively new and so far the focus has been on near-touching geometries [17,20].

Recently, we took a first step in applying an asymptotic approach to the analysis of the plasmonic properties of slender nanometallic structures [39]. In particular, we developed an approximate theory of the longitudinal plasmonic resonances of slender bodies of revolution, with the thickness profile along the symmetry axis being essentially arbitrary. Aside from key scalings, new closed-form approximations for special geometries and physical insight into the role of slenderness and shape, this work furnished a versatile semi-analytical scheme which allows one to rapidly calculate the plasmonic response of a certain family of complex three-dimensional (3D) geometries.

The framework in [39] is underpinned by a spectral theory which is exact in the quasistatic approximation; it is based on the so-called plasmonic eigenvalue problem [2,40–42], which defines a set of material- and frequency-independent modes of a nanometallic structure based on its geometry, with the relative permittivity of the structure playing the eigenvalue role. Given this set of modes, calculating the optical response of the structure for arbitrarily prescribed radiation sources and physical values of the particle permittivity amounts to the evaluation of normalization and overlap integrals involving the modes and the incident radiation field. At near-resonance frequencies, often a single mode dominates the spectral expansion; this modal approach is accordingly both efficient and insightful in that it provides a linkage between physical resonances and mathematical eigenfunctions.

In [39], we used asymptotic tools to calculate modes as well as overlap integrals. In particular, to analyze the plasmonic eigenvalue problem, we relied mainly on the method of matched asymptotic expansions, where the physical domain is decomposed into distinguished regions which are separately analyzed and then matched together; the use of such methodology in the context of slender particles is especially popular in fluid dynamics, where it is known as “slender-body theory” [43–48]. This allowed us to reduce the plasmonic eigenvalue problem for the body of revolution (restricted to the longitudinal, in this case axisymmetric, modes) to an asymptotically equivalent 1D problem whose domain is a finite line segment corresponding to the body’s centerline. In this reduced problem, the eigenvalue is the original permittivity eigenvalue scaled by κ^2 . With that rescaling, the

reduced problem involves κ only weakly, namely, through its logarithm. The eigenfunctions in the reduced problem represent effective 1D voltage and polarization-charge profiles. From these profiles, the corresponding mode distributions can be evaluated in 3D, everywhere in the interior and exterior of the particle; they can also be used to easily evaluate the normalization and overlap integrals appearing in the spectral formulation. The reduced eigenvalue problem consists of a differential equation which is coupled to an integral equation. The differential equation represents an effective Gauss law for an infinitesimal longitudinal segment of the body. (The boundary conditions are dependent on the local geometry of the tips.) The integral equation represents a spatially nonlocal capacity relation accounting for electrostatic interactions between different longitudinal segments of the body.

The purpose of this work is to extend the plasmonic slender body in [39] to slender nanometallic rings and configurations thereof. By a slender ring we mean a body whose thickness about a circular curve is small relative to the radius of that circle. We shall allow azimuthal variations in thickness and noncircular cross-sectional shapes, thus going considerably beyond the idealized case of a slender torus; we shall also consider ring dimers and chains, the separation between the rings being comparable to their radii. An obvious source of motivation for focusing on ring structures is that they are commonly employed in nanoplasmonics [49]; they are moderately compact, as discussed above, relatively easy to fabricate [50], their hollow center is advantageous for sensing applications [32,51] and offer increased tuning through aspect ratio [32,49], azimuthal thickness profile [52,53], and multiple-ring interactions [54–57]. We also have technical reasons to focus on ring geometries. Thus, the absence of tips eliminates the need to derive boundary conditions to close the reduced eigenvalue problem, which is generally quite a subtle aspect of the theory. Furthermore, the fact that rings degenerate to circular curves in the high-aspect-ratio limit will be seen to enable convenient diagonalizations of the integral operators appearing in the reduced problem.

The rest of the paper is structured as follows. In Sec. II, we formulate the general problem of scattering of a plane wave from a nanometallic structure in the quasistatic approximation and then review the plasmonic eigenvalue problem and its use for solving that scattering problem. In Sec. III, we employ asymptotic arguments in the high-aspect-ratio limit to derive a reduced eigenvalue problem in the case of a single ring; at this stage, we assume circular cross sections, although the thickness may vary in the azimuthal direction. To emphasize the physics, the asymptotic arguments are described intuitively and in dimensional notation; readers requiring a more formal justification of the approximations can refer to the derivation of the reduced problem in [39] and textbooks describing the method of matched asymptotic expansions and slender-body theory [38]. In the remainder of Sec. III, we discuss the singular scaling of the permittivity eigenvalues, the accuracy of the approximation scheme, and develop closed-form solutions for torus-shaped rings and a semianalytical scheme for azimuthally nonuniform rings. In Sec. IV, we generalize the reduced eigenvalue problem to the case of ring dimers, develop closed-form solutions for coaxial dimers formed of torus-shaped rings and a semi-analytical scheme for more

general dimer geometries. In Sec. V, we briefly discuss further geometrical extensions to noncircular cross sections and chains of rings; the latter extension is illustrated by considering the consequences of a defect in a coaxial chain of ring dimers. In Sec. VI, we demonstrate the application of the asymptotic modes to calculate absorption cross sections for ring configurations illuminated by a plane wave. In Sec. VII, we discuss limits of validity of the quasistatic approximation specifically in describing the longitudinal resonances of slender-ring structures, and show comparisons with full-wave simulations. We give concluding remarks in Sec. VIII.

II. QUASISTATIC FORMULATION

A. Scattering problem

Consider a homogeneous nanometallic structure in vacuum. We assume that the characteristic linear dimension of the structure is sufficiently small relative to the free-space wavelength such that a quasistatic approximation is applicable ([35], cf. Sec. VII). In what follows, we formulate a scattering problem governing the electric near field in the vicinity of the structure in the scenario where the structure is illuminated by a plane wave; for simplicity, we do not include in the formulation the possibility of near-field external sources.

In the quasistatic approximation, the electric field is irrotational in the vicinity of the structure. Defining this near field to be the real part of $\mathbf{E}e^{-i\omega t}$, wherein ω is angular frequency and t time, we may accordingly introduce an electric potential φ such that $\mathbf{E} = -\nabla\varphi$. Given the absence of near-field external sources, the potential φ satisfies

$$\nabla \cdot (\epsilon \nabla \varphi) = 0, \quad (2.1)$$

where ϵ denotes the permittivity relative to vacuum. In the exterior of the structure, $\epsilon = 1$. In the interior of the structure, ϵ is given by the complex-valued and frequency-dependent relative permittivity of the metal, say $\epsilon_r(\omega)$, for which empirical data are available (e.g., [58]). Alternatively, we may refer to the Drude model [1]

$$\epsilon_r(\omega) = 1 - \frac{\omega_p^2}{\omega^2 + i\gamma\omega}, \quad (2.2)$$

wherein ω_p is the plasma frequency and γ is a parameter representing Ohmic losses. The Drude model is adequate for frequencies considerably lower than ω_p , which as we shall see is the case for the longitudinal resonances of slender-ring structures. This model will be used for the sake of illustration in Sec. VI.

The quasistatic formulation is closed by the far-field condition

$$\mathbf{E} \rightarrow \mathbf{E}_\infty \quad \text{as} \quad |\mathbf{x}| \rightarrow \infty, \quad (2.3)$$

where the constant vector \mathbf{E}_∞ represents the incident plane wave. Specifically, keeping in mind that the near-field domain is small relative to the free-space wavelength, \mathbf{E}_∞ is the electric-field phasor of the incoming wave evaluated at the location of the structure.

B. Plasmonic eigenvalue problem

Upon setting \mathbf{E}_∞ to zero, (2.1) and (2.3) give the so-called ‘‘plasmonic eigenvalue problem’’ governing the localized-

surface-plasmon resonances of the nanometallic structure. Since frequency enters this problem solely via the metal permittivity ϵ_r , it is natural to take ϵ_r as the eigenvalue, henceforth denoted \mathcal{E} , rather than the frequency. The permittivity eigenvalues are scale invariant and independent of material and frequency; they are determined solely by the geometry of the structure. For a smooth geometry, there are infinitely many negative-real permittivity eigenvalues which accumulate at -1 [2,40,41,59]. The associated field distributions, namely eigenfunctions, are also scale invariant up to a linear stretching and can always be chosen real valued.

Physically, the eigenfunctions can be interpreted as perpetual localized-surface-plasmon oscillations in the absence of material losses and external forcing. (Radiation losses are effectively neglected in the quasistatic approximation.) Mathematically, the set of eigenfunctions possesses completeness and orthogonality properties that can be used to explicitly solve arbitrary scattering problems. In particular, the solution to the scattering problem formulated above can be written as the spectral expansion (see [2,41,42,60,61])

$$\begin{aligned} \varphi(\mathbf{x}) = & -\mathbf{E}_\infty \cdot \mathbf{x} + \sum_{l \in \mathcal{I}} \frac{\epsilon_r(\omega) - 1}{\epsilon_r(\omega) - \mathcal{E}^{(l)}} \frac{\int dV \mathbf{E}_\infty \cdot \nabla \varphi^{(l)}}{\int dV \nabla \varphi^{(l)} \cdot \nabla \varphi^{(l)}} \\ & \times \varphi^{(l)}(\mathbf{x}), \end{aligned} \quad (2.4)$$

where \mathcal{I} is an index set for the eigenvalues and eigenfunctions, dV is a volume element, and the integrals are over the interior of the structure. The integrals in the numerator and denominator are called overlap and normalization integrals, respectively. We note that scattering problems involving near-field sources can be treated similarly, with \mathbf{E}_∞ replaced by the total field in the absence of the structure. From (2.4), quasistatic approximations for the optical cross sections can be readily calculated, as we shall see in Sec. VI.

For frequencies such that the complex-valued permittivity $\epsilon_r(\omega)$ is close to a permittivity eigenvalue, the corresponding term in the expansion (2.4), or terms, in the case of perfect or near-perfect degeneracy, may become dominant. In that case, we say that the associated eigenfunctions (or eigenmodes) are resonantly excited by the incident radiation. Thus, for such near-resonance frequencies, the spectral solution can be asymptotically simplified, revealing a connection between the physical and mathematical perspectives described above. The existence and characteristics of such resonances in practice, however, depend on several additional factors including the relative smallness of the imaginary component of $\epsilon_r(\omega)$, the overlap between the incident field and the eigenfunctions participating in the resonance, as well as interference effects. All of these dependencies can be studied using (2.4) once the eigenvalues and eigenfunctions of the geometry have been calculated.

III. LONGITUDINAL MODES OF A SINGLE SLENDER RING

A. Geometry

In this section we consider the plasmonic eigenvalue problem (cf. Sec. IIB) in the case of a single nanosized ring of radius a and characteristic thickness b . For now, we assume that the ring is formed of circular cross sections of radius

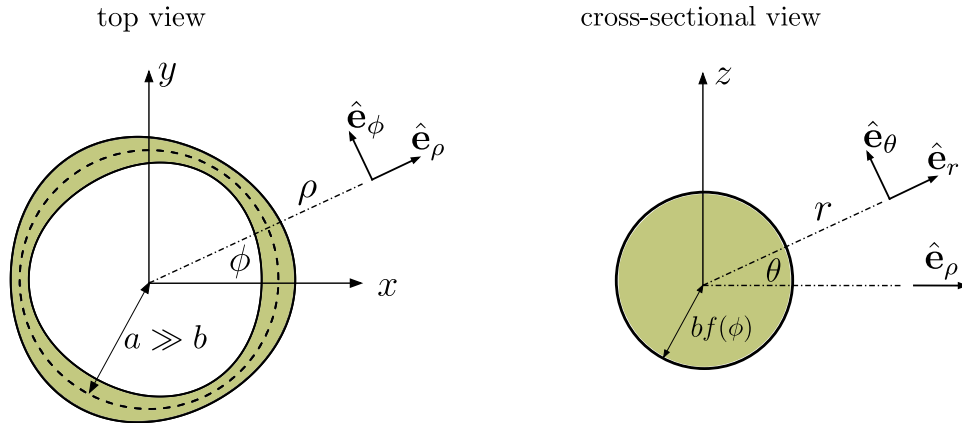


FIG. 1. Schematic of a slender ring with circular cross sections as considered in Sec. III.

$bf(\phi)$, which are centered about a circular centerline of radius a ; the thickness profile $f(\phi)$ is a dimensionless function of the azimuthal angle ϕ . (Noncircular cross sections are treated in Sec. V A.) In Fig. 1, we define the Cartesian (x, y, z) , cylindrical (ρ, z, ϕ) , and “cross-sectional” (r, θ, ϕ) coordinate systems. Accordingly, the position measured from the center of the ring can be written $\mathbf{x} = \mathbf{y} + r\hat{\mathbf{e}}_r$, where $\hat{\mathbf{e}}_r = \hat{\mathbf{e}}_\rho \cos \theta + \hat{\mathbf{e}}_z \sin \theta$ and $\mathbf{y}(\phi) = a\hat{\mathbf{e}}_\rho$ is the circular centerline, with $\hat{\mathbf{e}}_\rho = \hat{\mathbf{e}}_x \cos \phi + \hat{\mathbf{e}}_y \sin \phi$. Furthermore, the ring boundary can be written $r = bf(\phi)$.

B. Reduced eigenvalue problem

Henceforth, we consider slender rings for which the aspect ratio $\kappa = a/b$ is large and $f(\phi)$ is of order unity. In particular, our interest is in modes, i.e., solutions of the plasmonic eigenvalue problem, for which $\mathcal{E} \rightarrow -\infty$ as $\kappa \rightarrow \infty$. [According to the Drude model (2.2), large-negative permittivity eigenvalues imply low frequencies $\omega \ll \omega_p$.] For any mode with this asymptotic property, scaling arguments suggest that, as $\kappa \rightarrow \infty$, cross-sectional variations of the interior potential become negligible relative to azimuthal variations. We accordingly label such modes “longitudinal.” We note that in the case of a body of revolution [39], those modes can be identified based on symmetry as they simply correspond to the axisymmetric modes.

In light of the above, we approximate the interior potential as

$$\varphi(\mathbf{x}) = v(\phi), \quad (3.1)$$

where the azimuthal function $v(\phi)$ represents the voltage relative to infinity. (Without loss of generality, we take the potential to vanish at infinity.) Another key azimuthal function is the polarization-charge line density

$$q(\phi) = \oint_{r=bf(\phi)} dl \sigma, \quad (3.2)$$

where $\sigma = \epsilon_0[\mathbf{E} \cdot \hat{\mathbf{n}}]_i^e$ is the polarization-charge surface density, dl is a differential length element, and the integral is over the circular cross-sectional interface $r = bf(\phi)$ at constant ϕ ; in the expression for σ , ϵ_0 is the permittivity of vacuum, $\hat{\mathbf{n}}$ an outward normal unit vector, and the square brackets stand for the jump across the interface in that direction, the

subscript i and superscript e indicating the interior and exterior sides, respectively. For $|\mathcal{E}| \gg 1$, continuity of electrical displacement indicates that the interior normal field is negligible compared to the exterior normal field. We therefore make the approximation

$$\sigma = \epsilon_0(\mathbf{E} \cdot \hat{\mathbf{n}})_e, \quad (3.3)$$

the e subscript indicating evaluation on the exterior side of the interface.

Consider now the potential distribution in the exterior of the ring, specifically at distances from the centerline comparable with the characteristic thickness b . In that neighborhood of the ring boundary, the exterior potential can be approximated as

$$\varphi(\mathbf{x}) = -\frac{q(\phi)}{2\pi\epsilon_0} \ln \frac{r}{bf(\phi)} + v(\phi). \quad (3.4)$$

Namely, in any given cross-sectional plane, the exterior potential is locally provided by the potential distribution around an infinite, perfectly conducting, cylinder, which coincides with the ring in that plane and is held at a potential $v(\phi)$. In light of (3.3), the electrostatic surface-charge density at the cylinder boundary is nothing but the polarization surface-charge density σ , hence, the cylinder’s net apparent surface charge, per unit length, is $q(\phi)$. Lastly, the absence of θ -dependent solutions in (3.4) can be justified based on the circular shape of the boundary, the uniform potential prescribed on that boundary, as well as the anticipation that the potential gradient is negligible in the azimuthal direction and decays away from the ring’s centerline.

We shall now derive two relations between $v(\phi)$ and $q(\phi)$. The first is based on Gauss law, which in the absence of free charge reduces to [cf. (2.1)]

$$\oint dA \epsilon_0 \epsilon \mathbf{E} \cdot \hat{\mathbf{n}} = 0, \quad (3.5)$$

where dA is a differential area element, $\hat{\mathbf{n}}$ is an outward normal unit vector, and the integral is over an arbitrary closed surface. Consider that closed surface to be the boundary of a curved tube, which closely encloses a segment of the ring between the cross-sectional planes $\phi = \phi'$ and $\phi = \phi' + \Delta\phi$. From (3.2) and (3.3), the contribution to the integral from the part of the tube boundary that lies outside the ring is

$aq(\phi')\Delta\phi$. Since the interior azimuthal field is approximately uniform over the cross section, we find that the contribution from the part of the tube boundary that lies inside the ring, namely, the end faces, is

$$\epsilon_0\mathcal{E}\{(A\mathbf{E}\cdot\hat{\mathbf{e}}_\phi)_{\phi'+\Delta\phi}-(A\mathbf{E}\cdot\hat{\mathbf{e}}_\phi)_{\phi'}\}, \quad (3.6)$$

where A denotes the cross-sectional area. By taking the limit $\Delta\phi\rightarrow 0$, using (3.1), we find the effective Gauss law

$$\frac{q}{\epsilon_0}=\frac{\mathcal{E}}{\kappa^2}\frac{d}{d\phi}\left(\bar{A}\frac{dv}{d\phi}\right), \quad (3.7)$$

where we define the scaled cross-sectional area $\bar{A}=A/b^2$. In the present case, where the cross-sectional shape is circular, $\bar{A}=\pi f^2$.

The second relation arises from the need to resolve the logarithmic growth of the exterior potential away from the centerline of the ring. This is done by matching (3.4) with an approximation for the exterior potential that holds at distances from the centerline that are comparable to a . Thus, on the latter scale, the finite thickness of the ring is indiscernible and the potential is approximated as that of a circular wire of charge line density $q(\phi)$, viz.,

$$\varphi(\mathbf{x})=\frac{a}{4\pi\epsilon_0}\int_0^{2\pi}d\phi'\frac{q(\phi')}{|\mathbf{x}-\mathbf{y}(\phi')|}. \quad (3.8)$$

We then compare (3.4) with the behavior of (3.8) close to the centerline, which is derived in Appendix A, to derive the matching condition

$$v(\phi)=\frac{q(\phi)}{2\pi\epsilon_0}\ln\frac{8\kappa}{f(\phi)}+\frac{1}{4\pi\epsilon_0}\int_0^{2\pi}d\phi'\frac{q(\phi')-q(\phi)}{2\sin\frac{|\phi-\phi'|}{2}}, \quad (3.9)$$

which is an integral capacitance relation between the voltage at a given azimuthal angle ϕ and the azimuthal distribution of polarization charge over the entire ring.

The differential Gauss law (3.7) and the integral capacitance relation (3.9) together constitute a ‘‘reduced eigenvalue problem’’ for the ‘‘reduced eigenvalue’’ \mathcal{E}/κ^2 and ‘‘reduced eigenfunctions’’ $v(\phi)$ and $q(\phi)/\epsilon_0$, which are 2π -periodic functions of ϕ . Like the exact plasmonic eigenvalue problem, this reduced problem is purely geometric; in particular, the geometry enters through the thickness profile $f(\phi)$ and the logarithm of the aspect ratio κ .

C. ‘‘Logarithmically approximated’’ solutions to the reduced eigenvalue problem

Before attempting to solve the reduced eigenvalue problem in its present form, it is insightful to discuss a coarse ‘‘logarithmic’’ approximation of the reduced problem which is based on the formal largeness of $\ln\kappa$ as $\kappa\rightarrow\infty$. In this approximation, the integral capacitance relation (3.9) reduces to the algebraic relation

$$q/\epsilon_0\approx\frac{2\pi}{\ln\kappa}v. \quad (3.10)$$

Substituting (3.10) into the Gauss law (3.7) then gives

$$-\frac{\mathcal{E}}{\kappa^2}\frac{d}{d\phi}\left(\bar{A}\frac{dv}{d\phi}\right)+\frac{2\pi}{\ln\kappa}v\approx 0, \quad (3.11)$$

to be solved together with the periodic boundary conditions on v .

The simplified model (3.11) clearly implies the asymptotic scaling

$$\mathcal{E}\simeq\frac{\kappa^2}{\ln\kappa}\quad\text{as}\quad\kappa\rightarrow\infty, \quad (3.12)$$

which slightly differs from the usually quoted scaling for slender geometries mentioned in the introduction by the logarithmic factor; we note that the same scaling was found in [39] for the longitudinal modes of slender bodies of revolution. In particular, consider the case of a torus-shaped ring, with b identified as the cross-sectional radius. Then $\bar{A}(\phi)\equiv\pi$ and solving (3.11) yields the approximate eigenvalues

$$\mathcal{E}^{(m)}\approx-\frac{2\kappa^2}{m^2\ln\kappa},\quad m=1,2,\dots \quad (3.13)$$

with corresponding pairs of independent eigenfunctions

$$v^{(m,c)}\approx\cos m\phi,\quad v^{(m,s)}\approx\sin m\phi, \quad (3.14a,b)$$

the degeneracy being induced by symmetry. The corresponding polarization-charge eigenfunctions $q^{(m,c)}$ and $q^{(m,s)}$ can readily be deduced from (3.10).

The above scheme corresponds to a leading-order approximation in a perturbative expansion in inverse powers of $\ln\kappa$. In particular, the relative error in (3.13) is on the order of $1/\ln\kappa$. In slender-body theory, such logarithmic approximations are often referred to as ‘‘local slender-body theory.’’ This should be contrasted with the nonapproximated reduced eigenvalue problem, which constitutes a ‘‘nonlocal slender-body theory,’’ the term ‘‘nonlocal’’ here referring to the integral capacitance relation (3.9). It can be shown that the reduced eigenvalue problem effectively sums the logarithmic expansion mentioned above, resulting in solutions which are ‘‘algebraically’’ accurate, i.e., involving relative errors which are asymptotically smaller than some negative power of κ . The distinction between local and nonlocal slender-body theory should not be confused with the notion of spatial nonlocality of the metal’s dielectric function, which we do not address in this paper.

D. ‘‘Exact’’ solutions to the reduced eigenvalue problem

1. Diagonalization of the self-interaction integral operator

We now proceed to derive ‘‘exact’’ solutions to the reduced eigenvalue problem [cf. (3.7) and (3.9)], i.e., without exploiting the formal largeness of $\ln\kappa$. An essential step is to note that the integral operator appearing in the capacitance relation (3.9) is diagonalized by the set of Fourier eigenfunctions. Specifically, for any integer m ,

$$\int_0^{2\pi}d\phi'\frac{e^{im\phi'}-e^{im\phi}}{2\sin\frac{|\phi'-\phi|}{2}}=\lambda_me^{im\phi}, \quad (3.15)$$

with $\lambda_0=0$ and

$$\lambda_m=-4\sum_{k=1}^{|m|}\frac{1}{2k-1}\quad\text{for}\quad m=\pm 1,\pm 2,\dots \quad (3.16)$$

A proof of this result is given in Appendix B.

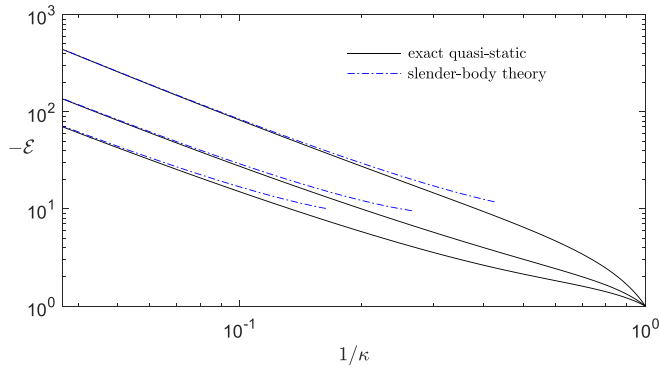


FIG. 2. Three lowest permittivity eigenvalues, not counting multiplicities, of a torus-shaped ring as a function of the reciprocal of its aspect ratio κ : exact solutions of the quasistatic plasmonic eigenvalue problem [33] vs the slender-body approximation (3.17).

2. Torus-shaped rings

We first consider the case of torus-shaped rings, for which f and \bar{A} are independent of ϕ . Identifying the cross-sectional radius as b , we have $f(\phi) \equiv 1$ and $\bar{A}(\phi) \equiv \pi$. (Henceforth, we will always adopt this convention when referring to torus-shaped rings.) For constant \bar{A} , the same set of Fourier eigenfunctions that diagonalizes the integral operator in the capacitance relation (3.9) as in (3.15) also diagonalizes the differential operator in the Gauss law (3.7) since $d^2 e^{im\phi} / d\phi^2 = -m^2 e^{im\phi}$. Furthermore, for constant f , the logarithmic factor multiplying $q(\phi)$ in (3.9) reduces to a constant. Accordingly, it is immediate to deduce the eigenvalues

$$\mathcal{E}^{(m)} = -\frac{2\kappa^2}{m^2} \left(\ln 8\kappa - 2 \sum_{k=1}^m \frac{1}{2k-1} \right)^{-1} \quad \text{for } m = 1, 2, \dots, \quad (3.17)$$

with associated voltage eigenfunctions

$$v^{(m,c)} = \cos m\phi, \quad v^{(m,s)} = \sin m\phi. \quad (3.18a,b)$$

The closed-form expression (3.17) constitutes an algebraically accurate slender-body approximation for the reduced eigenvalues of a torus-shaped ring. It is asymptotically consistent with, and improves on, the corresponding logarithmically accurate approximation (3.13). Surprisingly, the algebraically accurate voltage eigenfunctions (3.18) are of the same form as the logarithmically accurate eigenfunctions (3.14). The algebraically accurate relation between the voltage and polarization-charge eigenfunctions, however, reads as

$$q^{(m,c)} / \epsilon_0 = 2\pi \left(\ln 8\kappa - 2 \sum_{k=1}^m \frac{1}{2k-1} \right)^{-1} v^{(m,c)}, \quad (3.19)$$

which should be compared with the corresponding logarithmically accurate relation (3.10).

In the present case of a torus-shaped ring, exact solutions of the plasmonic eigenvalue problem can be obtained by separation of variables in toroidal coordinates [33]. In Fig. 2, we compare the first three eigenvalues, not counting multiplicities, computed in this manner with the corresponding values predicted by the slender-body approximation (3.17).

As expected, the slender-body approximations approach the computed eigenvalues as $\kappa \rightarrow \infty$.

At the same time, the comparison in Fig. 2 demonstrates the fact that, for fixed κ , the slender-body approximation deteriorates in accuracy with increasing mode number; conversely, as the mode number increases, accuracy can be retained only by increasing κ . This is not surprising given that our slender-body approximation corresponds to a limit process where $\kappa \rightarrow \infty$ for a fixed mode; there is therefore no reason to expect the approximation to hold in the double limit where both κ and m are large [39]. In fact, the scale on which the voltage and charge eigenfunctions vary along the ring, assumed large compared to the ring thickness in the slender-body approximation, becomes comparable to the ring thickness for $m \simeq \kappa$; moreover, for such large m , (3.17) gives $|\mathcal{E}^{(m)}| \simeq 1$, whereas the theory relies on the permittivity contrast being large. We note that this limitation of the theory does not interfere with our goal of describing the low-order (low-frequency) longitudinal resonances of slender nanometallic rings.

The remainder of this section and the next two sections are concerned with extensions of the slender-body theory derived so far to the calculation of the longitudinal modes of more general ring geometries, including azimuthally nonuniform rings, ring dimers, and chains and rings with noncircular cross sections. Some readers may prefer at this point to jump to Sec. VI, where we illustrate the application of the slender-body theory to the solution of the quasistatic scattering problem formulated in Sec. II.

3. Rings of nonuniform thickness

Consider now rings for which the thickness profile f depends on the azimuthal angle ϕ . In this more general case, we solve the reduced eigenvalue problem using a semianalytical method, which is based on approximating the reduced eigenfunctions $v(\phi)$ and $q(\phi)$ by the truncated Fourier series

$$v = \sum_{k=0}^K \{ \alpha_k \cos k\phi + \beta_k \sin k\phi \},$$

$$\frac{q}{\epsilon_0} = \sum_{k=1}^K \{ \tilde{\alpha}_k \cos k\phi + \tilde{\beta}_k \sin k\phi \}, \quad (3.20a,b)$$

where $K \in \mathbb{N}$ is a truncation parameter discussed below. Note that the zeroth harmonic is omitted from the charge representation (3.20b) in accordance with the zero-net-charge constraint $\int_0^{2\pi} d\phi q = 0$, which readily follows from integration of Gauss law (3.7). With (3.20), Fourier projection of the capacitance relation (3.9) and Gauss law (3.7) yields a $2K \times 2K$ generalized eigenvalue problem of the form

$$\mathbf{q} = -\bar{\mathcal{E}} \mathbf{M} \cdot \mathbf{v}, \quad \mathbf{v} = \mathbf{U} \cdot \mathbf{q}, \quad (3.21a,b)$$

where $\mathbf{v} = (\alpha_1, \dots, \alpha_K, \beta_1, \dots, \beta_K)^T$ and $\mathbf{q} = (\tilde{\alpha}_1, \dots, \tilde{\alpha}_K, \tilde{\beta}_1, \dots, \tilde{\beta}_K)^T$, with T denoting the vector transpose; we have introduced the notation $\bar{\mathcal{E}} = \mathcal{E} / \kappa^2$ for the reduced eigenvalue; and the matrices \mathbf{M} and \mathbf{U} are provided in Appendix C, along with an expression for the coefficient α_0 , which is computed *a posteriori*. As already mentioned, the slender-body approximation cannot be expected to correctly capture thickness-scale variations in the

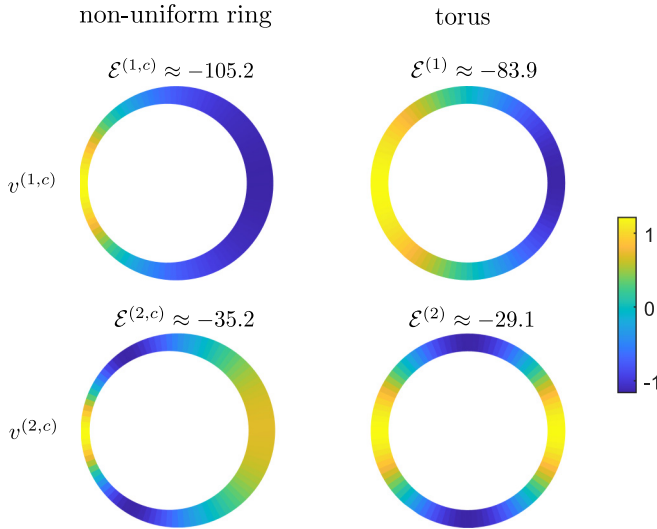


FIG. 3. Slender-body approximations for the “dipolar” (1, c) and “quadrupolar” (2, c) voltage eigenfunctions and associated eigenvalues of a torus-shaped ring and an azimuthally nonuniform ring with thickness profile $f(\phi) = 1 + 0.5 \cos \phi$; for both geometries $\kappa = 10$.

longitudinal direction. In fact, the reduced formulation can be shown to be ill posed for $K \simeq \kappa$ [62]. Accordingly, the truncation parameter K should be chosen much smaller than κ . Of course, K should also be chosen larger than the number of modes to be resolved.

In contrast to the case of a torus-shaped ring, it is clear from the above scheme that for a nonuniform ring each mode generally contains multiple Fourier harmonics. In particular, whereas for a torus-shaped ring only modes (1, c) and (1, s), which share the degenerate eigenvalue $\mathcal{E}^{(1)}$, are “dipolar,” i.e., include a first Fourier harmonic, for nonuniform rings generally all modes include a dipolar component. As we shall see in Sec. VI, this observation is important for interpreting the differences between the resonant response of uniform and nonuniform rings under plane-wave illumination.

As an example, we consider an azimuthally nonuniform ring whose thickness profile is $f = 1 + 0.5 \cos \phi$. The voltage eigenfunctions can be classified as being either even or odd with respect to the symmetry plane of the geometry which is normal to the plane of the ring; referring to (3.20a), these modes are, respectively, comprised of either only cosine or only sine Fourier components. Consistently with our notation for the longitudinal modes of a torus-shaped ring [cf. (3.18)], we denote the m th even mode by the superscript (m, c); similarly, the m th odd mode by the superscript (m, s). In Fig. 3, we show for $\kappa = 10$ the “dipolar” (1, c) and “quadrupolar” (2, c) modes of a torus-shaped ring, along with the corresponding modes of the azimuthally nonuniform ring. In the latter case, the modes are computed by solving (3.21) with $K = 6$.

IV. LONGITUDINAL MODELS OF RING DIMERS

In this section we consider the longitudinal modes of ring dimers. In Sec. IV A, we generalize the reduced eigenvalue problem derived in Sec. III B for a single ring to the dimer case. In Sec. IV B, we obtain exact closed-form solutions

to the generalized reduced problem in the case of a dimer formed of coaxial, generally dissimilar, torus-shaped rings. In Sec. IV C, we consider more general ring dimers using a semi-analytical scheme (we also present an *ad hoc* approximation which is in some cases suitable). As we will demonstrate in Sec. V, configurations of more than two rings can be handled similarly.

A. Reduced eigenvalue problem for ring dimers

We adopt the same notation as in Sec. III, only with subscripts added to indicate to which ring a given quantity is associated with. By revisiting the derivation in Sec. III, we find that in the thickness-scale vicinity of the rings we have the local approximation

$$\varphi(\mathbf{x}) = -\frac{q_n(\phi)}{2\pi\epsilon_0} \ln \frac{r}{b_n f_n(\phi)} + v_n(\phi), \quad n = 1, 2 \quad (4.1)$$

for the exterior potential, which generalizes (3.4). Similarly, the effective Gauss law (3.7) now applies to each ring separately:

$$\frac{q_n}{\epsilon_0} = \frac{\mathcal{E}}{\kappa_n^2} \frac{d}{d\phi} \left(\bar{A}_n \frac{dv_n}{d\phi} \right), \quad n = 1, 2. \quad (4.2)$$

It remains to generalize the integral capacitance relation (3.9). To this end, consider the ring-scale exterior potential (3.8), which generalizes as

$$\varphi(\mathbf{x}) = \sum_{n=1,2} \frac{a_n}{4\pi\epsilon_0} \int_0^{2\pi} d\phi' \frac{q_n(\phi')}{|\mathbf{x} - \mathbf{y}_n(\phi')|}. \quad (4.3)$$

Using the results of Appendix A to match (4.3) and (4.1), we find the coupled pair of integral capacitance relations

$$\begin{aligned} v_n(\phi) = & \frac{q_n(\phi)}{2\pi\epsilon_0} \ln \frac{8\kappa_n}{f_n(\phi)} + \frac{1}{4\pi\epsilon_0} \int_0^{2\pi} d\phi' \frac{q_n(\phi') - q_n(\phi)}{2 \sin \frac{|\phi' - \phi|}{2}} \\ & + \frac{a_k}{4\pi\epsilon_0} \int_0^{2\pi} d\phi' \frac{q_k(\phi')}{|\mathbf{y}_n(\phi) - \mathbf{y}_k(\phi')|}, \end{aligned} \quad (4.4)$$

for $(n, k) = (1, 2)$ and $(2, 1)$.

The differential equations (4.2) and integral equations (4.4) together constitute a generalized reduced eigenvalue problem for ring dimers. We see that the rings interact solely through the last “coupling” integral on the right-hand side of (4.4), whereby the polarization-charge distribution of one ring induces a voltage disturbance in the other ring, and vice versa.

B. Coaxial rings

1. Diagonalization of the coupling integral operator

For coaxial rings, the coupling-integral operator in (4.4) is diagonalized by the same Fourier basis that diagonalizes the self-interaction integral operator as in (3.15). Indeed, in this case, the distance between the point on the centerline of ring 1 at azimuthal angle ϕ_1 and the point on the centerline of ring 2 at azimuthal angle ϕ_2 can be written $|\mathbf{y}_1(\phi_1) - \mathbf{y}_2(\phi_2)| = D(\phi_1 - \phi_2)$, where $D(u) = \sqrt{h^2 + a_1^2 + a_2^2 - 2a_1 a_2 \cos u}$, h being the vertical distance between the rings. Since $D(u)$ is even, periodic, and positive, its reciprocal can be expanded as

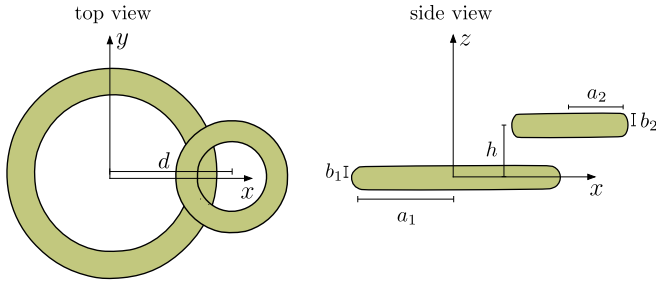


FIG. 4. Schematic of a bilayer dimer of torus-shaped rings. The rings have centerline radii a_1 and a_2 , and aspect ratios $\kappa_1 = a_1/b_1$ and $\kappa_2 = a_2/b_2$. The horizontal and vertical separation between the rings is d and h , respectively. The coaxial case considered in Sec. IV B corresponds to the case $d = 0$. The noncoaxial case $d \neq 0$ is considered in Sec. IV C.

a cosine Fourier series. It then readily follows that

$$\int_0^{2\pi} d\phi' \frac{e^{im\phi'}}{|\mathbf{y}_1(\phi) - \mathbf{y}_2(\phi')|} = \tau_m e^{im\phi} \quad \text{for } m = 0, \pm 1, \pm 2, \dots, \quad (4.5)$$

where

$$\tau_m = \int_0^{2\pi} du \frac{\cos mu}{D(u)}. \quad (4.6)$$

With (4.5), it is straightforward to generalize the semianalytical scheme of Sec. III D 3 to the case of arbitrary coaxial ring dimers. Instead, we shall focus in the present subsection on the case of coaxial dimers formed of torus-shaped, not necessarily identical, rings (see Fig. 4 for $d = 0$), where (4.5) actually facilitates the derivation of closed-form solutions. Later, in Sec. IV C, we will present a more general semianalytical scheme, not relying on (4.5), that applies to arbitrary ring dimers, including noncoaxial dimers formed of nonuniform rings.

2. Coaxial homodimers

Consider first the case of a coaxial homodimer, namely, a coaxial pair of identical torus-shaped rings ($a_1 = a_2 = a$, $\kappa_1 = \kappa_2 = \kappa$). Given the symmetries of the geometry, we anticipate eigenvalues $\mathcal{E}^{(m,\pm)}$, for $m = 1, 2, \dots$, with corresponding eigenfunctions

$$\begin{pmatrix} v_1^{(m,c,\pm)} \\ v_2^{(m,c,\pm)} \end{pmatrix} = \begin{pmatrix} 1 \\ \pm 1 \end{pmatrix} \cos m\phi, \quad \begin{pmatrix} v_1^{(m,s,\pm)} \\ v_2^{(m,s,\pm)} \end{pmatrix} = \begin{pmatrix} 1 \\ \pm 1 \end{pmatrix} \sin m\phi. \quad (4.7a,b)$$

The \pm modes are, respectively, even and odd about the plane equidistance between the rings; we shall also refer to these as in- and out-of-phase modes, respectively, as this will allow a generalized interpretation in the heterodimers case considered next. Writing the eigenfunctions as in (4.7), use of the diagonalization identities (3.15) and (4.5) readily yields

$$\mathcal{E}^{(m,\pm)} = -\frac{2\kappa^2}{m^2} \left(\ln 8\kappa - 2 \sum_{k=1}^m \frac{1}{2k-1} \pm \frac{\Delta_m}{2} \right)^{-1}, \quad (4.8)$$

where $\Delta_m = a\tau_m$ is a dimensionless function of the ratio $h' = h/a$ defined by the quadrature [cf. (4.6)]

$$\Delta_m(h') = \int_0^{2\pi} du \frac{\cos mu}{\sqrt{h'^2 + 2 - 2\cos u}}, \quad (4.9)$$

which determines the eigenvalue splitting induced by the interaction between the rings [cf. (3.17)].

The functions $\Delta_m(h')$ are positive. Hence, for any m , the in-phase modes are higher energy (less negative permittivity), as one would expect. Furthermore, the functions $\Delta_m(h')$ are monotonically decreasing, asymptotically like $\Delta_m = O(1/h^{2m+1})$ as $h' \rightarrow \infty$; this represents the approach to the eigenvalues (3.17) of a single torus-shaped ring. We also note that $\Delta_m(h')$ is logarithmically singular as $h' \rightarrow 0$, which is acceptable given that the theory only holds for $h \gg b$, i.e., $h' \gg 1/\kappa$. In particular, for $m = 1$ we find from (4.9) the behaviors

$$\begin{aligned} \Delta_1 &\sim -2 \ln h' + 6 \ln 2 - 4 \quad \text{as } h' \rightarrow 0, \\ \Delta_1 &\sim \frac{\pi}{h'^3} \quad \text{as } h' \rightarrow \infty. \end{aligned} \quad (4.10a,b)$$

In Fig. 5, the eigenvalues $\mathcal{E}^{(1,\pm)}$ of the in- and out-of-phase dipolar modes, calculated using (4.8), are depicted by the solid curves as a function of h/a , for $\kappa = 10$. Also shown are the asymptotic behaviors of the eigenvalues for small and large h/a , which follow from the behaviors (4.10).

3. Coaxial heterodimers

The above results are easily generalized to allow for dissimilar torus-shaped rings. Since the geometry remains azimuthally invariant, we look for voltage eigenfunctions of the form $\{v_1, v_2\} = \{c_1, c_2\} \times \cos m\phi$, in which c_1 and c_2 are constant prefactors and $m = 1, 2, \dots$. There are also $\pi/2$ rotations of these modes having the same eigenvalues. Using the diagonalization identities (3.15) and (4.5), we find that, for $m = 1, 2, \dots$, the reduced eigenvalue problem of Sec. IV A is transformed into the 2×2 matrix eigenvalue problem

$$\begin{pmatrix} c_1 \\ c_2 \end{pmatrix} = -\mathcal{E} \begin{pmatrix} \gamma_{1,1} & \gamma_{1,2} \\ \gamma_{2,1} & \gamma_{2,2} \end{pmatrix} \begin{pmatrix} c_1 \\ c_2 \end{pmatrix}, \quad (4.11)$$

in which the matrix on the right-hand side has the diagonal and nondiagonal elements

$$\gamma_{n,n} = \frac{m^2}{2\kappa_n^2} \left(\ln 8\kappa_n - 2 \sum_{k=1}^m \frac{1}{2k-1} \right), \quad \gamma_{n,k} = \frac{m^2}{4\kappa_k^2} (a_k \tau_m), \quad (4.12a,b)$$

respectively, where the products $a_k \tau_m$ are dimensionless geometric factors which determine the coupling between the rings [cf. (4.6)]. Solving the above system gives the eigenvalues

$$\mathcal{E}^{(m,\pm)} = -\frac{2}{\gamma_{1,1} + \gamma_{2,2} \pm \sqrt{(\gamma_{1,1} - \gamma_{2,2})^2 + 4\gamma_{1,2}\gamma_{2,1}}} \quad (4.13)$$

and corresponding eigenvectors

$$\begin{pmatrix} c_1^{(m,\pm)} \\ c_2^{(m,\pm)} \end{pmatrix} = \begin{pmatrix} \gamma_{1,2} \\ \frac{\gamma_{2,2} - \gamma_{1,1} \pm \sqrt{(\gamma_{1,1} - \gamma_{2,2})^2 + 4\gamma_{1,2}\gamma_{2,1}}}{2} \end{pmatrix}. \quad (4.14)$$

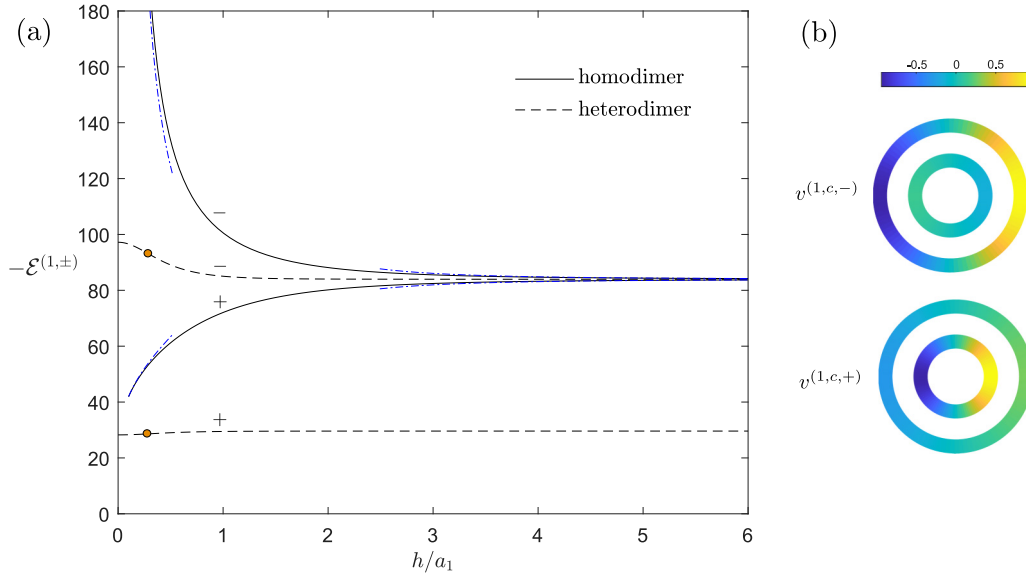


FIG. 5. (a) Eigenvalues of in- and out-of-phase dipolar modes of a coaxial homodimer ($\kappa = 10$) and heterodimer ($\kappa_1 = 10, \kappa_2 = 5, a_1/a_2 = 2$) as a function of the scaled vertical separation h/a_1 . The eigenvalues are calculated based on formulas (3.17) and (4.13) for the homodimer and heterodimer, respectively. The dashed-dotted lines depict the asymptotic behaviors implied by (4.10). (b) Corresponding cosine-dipolar voltage eigenfunctions in the heterodimer case, for $h/a_1 = 0.3$.

In summary, for $m = 1, 2, \dots$, there are two degenerate plasmonic eigenvalues $\mathcal{E}^{(m,\pm)}$, given by (4.13), with corresponding eigenfunctions

$$\begin{aligned} \begin{pmatrix} v_1^{(m,c,\pm)} \\ v_2^{(m,c,\pm)} \end{pmatrix} &= \begin{pmatrix} c_1^{(m,\pm)} \\ c_2^{(m,\pm)} \end{pmatrix} \cos m\phi, \\ \begin{pmatrix} v_1^{(m,s,\pm)} \\ v_2^{(m,s,\pm)} \end{pmatrix} &= \begin{pmatrix} c_1^{(m,\pm)} \\ c_2^{(m,\pm)} \end{pmatrix} \sin m\phi, \end{aligned} \quad (4.15a,b)$$

where $c_1^{(m,\pm)}$ and $c_2^{(m,\pm)}$ are given by (4.14).

It can be verified from the above results that $\mathcal{E}^{(m,+)} > \mathcal{E}^{(m,-)}$, namely, that for any given m the $+$ mode is higher energy than the $-$ mode. Furthermore, $c_1^{(m,\pm)}$ is positive, whereas $c_2^{(m,+)}$ and $c_2^{(m,-)}$ are positive and negative, respectively. The latter observation suggests referring to the \pm modes as in- and out-of-phase modes, respectively, consistently with the coaxial homodimer case. In contrast to the latter case, where the in- and out-of-phase labeling is associated with a mirror symmetry, here the voltage profile in one ring is not simply the same as or negative of that in the other. We shall see in Sec. VI that this distinction is important for interpreting the resonant response of coaxial dimers.

As an example, consider a coaxial heterodimer with $a_1/a_2 = 2$ and $b_1 = b_2$ (i.e., $\kappa_1 = 10$ and $\kappa_2 = 5$). In Fig. 5(a), the dashed curves depict the eigenvalues $\mathcal{E}^{(1,\pm)}$, calculated using (4.13), of the in- and out-of-phase dipolar modes of this coaxial heterodimer as a function of h/a_1 . The voltage profiles for the corresponding cosine-dipolar modes, for $h/a_1 = 0.3$, are shown in Fig. 5(b). Unlike in the coaxial-homodimer case also presented in that figure, the rings of the heterodimer do not become arbitrarily close as $h \rightarrow 0$, hence, the eigenvalues of the heterodimer approach finite values in that limit. Of course, we could have also considered a coaxial heterodimer formed of rings of similar radius yet different thickness, in

which case the eigenvalues would be singular as $h \rightarrow 0$, as in the coaxial-homodimer case.

C. Noncoaxial dimers

1. Semianalytical scheme

We now present a semianalytical scheme to solve the reduced eigenvalue problem of Sec. IV A in the case of an arbitrary ring dimer, meaning that the rings need not be coaxial, identical, nor azimuthally uniform. Following the derivation of the single-ring semianalytical scheme in Sec. III D 3, we represent the voltage and polarization-charge distributions in each ring by truncated Fourier series as in (3.20), with the Fourier coefficients now denoted $\alpha_{n,k}, \beta_{n,k}$, etc., with the first and second subscripts corresponding to the ring number and Fourier harmonic, respectively. With that representation, projection of the reduced eigenvalue problem on the truncated Fourier basis yields the $4K \times 4K$ generalized matrix-eigenvalue problem

$$\begin{aligned} \begin{pmatrix} \mathbf{q}_1 \\ \mathbf{q}_2 \end{pmatrix} &= -\bar{\mathcal{E}} \begin{pmatrix} \frac{\kappa_2}{\kappa_1} \mathbf{M}_1 & 0 \\ 0 & \frac{\kappa_1}{\kappa_2} \mathbf{M}_2 \end{pmatrix} \cdot \begin{pmatrix} \mathbf{v}_1 \\ \mathbf{v}_2 \end{pmatrix}, \\ \begin{pmatrix} \mathbf{v}_1 \\ \mathbf{v}_2 \end{pmatrix} &= \begin{pmatrix} \mathbf{U}_1 & \sqrt{\frac{a_2}{a_1}} \mathbf{V} \\ \sqrt{\frac{a_1}{a_2}} \mathbf{V}^T & \mathbf{U}_2 \end{pmatrix} \cdot \begin{pmatrix} \mathbf{q}_1 \\ \mathbf{q}_2 \end{pmatrix}, \end{aligned} \quad (4.16a,b)$$

where $\mathbf{v}_n = (\alpha_{n,1}, \dots, \alpha_{n,K}, \beta_{n,1}, \dots, \beta_{n,K})^T$ and $\mathbf{q}_n = (\tilde{\alpha}_{n,1}, \dots, \tilde{\alpha}_{n,K}, \tilde{\beta}_{n,1}, \dots, \tilde{\beta}_{n,K})^T$; $\bar{\mathcal{E}} = \mathcal{E}/(\kappa_1 \kappa_2)$ is a rescaled eigenvalue; \mathbf{M}_n and \mathbf{U}_n are identical to the matrices \mathbf{M} and \mathbf{U} , respectively, used in the single-ring scheme (3.21), with the geometric parameters being those of ring n ; and \mathbf{V} is a coupling matrix whose form is provided in Appendix C 2.

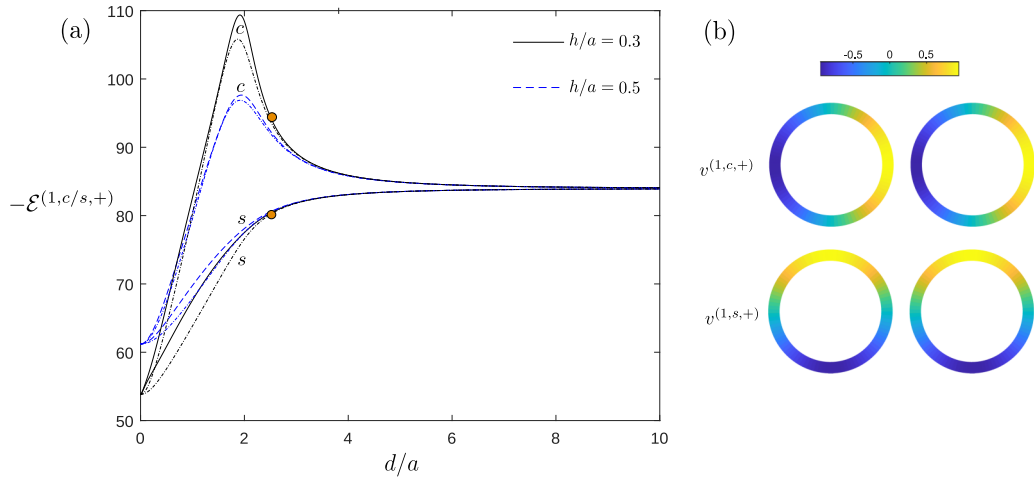


FIG. 6. (a) Eigenvalues $\mathcal{E}^{(1,c,+)}$ and $\mathcal{E}^{(1,s,+)}$ of the noncoaxial bilayer dimer shown in Fig. 4, in the case where the rings are identical ($\kappa = 10$). The eigenvalues, obtained by solving the semianalytical scheme (4.16), are plotted as a function of the scaled horizontal displacement d/a and for the indicated values of the relative vertical displacement h/a . Dashed-dotted curves depict the *ad hoc* analytical approximation (4.17). (b) Corresponding cosine-dipolar and sine-dipolar voltage eigenfunctions in the noncoaxial bilayer dimer for $d/a = 2.5$ and $h/a = 0.3$.

2. Noncoaxial homodimers

As an example of a noncoaxial dimer configuration, we consider the bilayer configuration shown in Fig. 4. It consists of a pair of torus-shaped rings whose centerlines define parallel planes separated by the vertical distance h , and whose symmetry axes are separated by the horizontal distance d . The case where d vanishes corresponds to the coaxial configuration considered in Sec. IV B, while the limit $h^2 + d^2 \rightarrow \infty$ corresponds to that of noninteracting rings. We have seen that both of these extreme cases are analytically solvable, with each longitudinal mode involving only a single Fourier harmonic. In contrast, in the general case each mode is expected to consist of a combination of Fourier harmonics. Symmetry still allows, however, the modes of the bilayer geometry to be classified based on whether the voltage eigenfunctions are even or odd about the x - z mirror plane. With the azimuthal angle ϕ measured from the x direction, these even and odd modes involve only cosine or sine Fourier harmonics, respectively. Thus, the semianalytical scheme (4.16) is reduced in this case to two uncoupled $2K \times 2K$ matrix problems.

We first consider the homodimer case where the rings are identical ($a_1 = a_2 = a$, $\kappa_1 = \kappa_2 = \kappa$). In particular, we focus attention on the two modes continued, as d is increased from zero, from the degenerate in-phase dipolar modes $(1, c, +)$ and $(1, s, +)$ found in the coaxial case (Sec. IV B 2). Figure 4 depicts the variation with d/a of the respective eigenvalues, say $\mathcal{E}^{(1,c,+)}$ and $\mathcal{E}^{(1,s,+)}$, calculated using the semianalytical scheme (4.16) for two values of h/a . Note that the “ c ” and “ s ” modes are even and odd about the x - z plane, respectively, as in the coaxial case, but are no longer degenerate rotations of each other. The insets show the voltage eigenfunctions for the indicated values of d/a and h/a .

A numerical study based on the semianalytical scheme (4.16) suggests that the modes of this bilayer homodimer configuration are, by visual inspection, dominated by a single Fourier harmonic. This harmonic corresponds to that of the mode of the corresponding coaxial (or isolated-ring) configuration from which the bilayer mode is continued from. This observation suggests an intuitive and *ad hoc* approximation in which the voltage profiles in both rings are constructed from just the apparently dominant harmonic. With that assumption, we obtain

$$\mathcal{E}^{(m,c,\pm)} \approx -\frac{2\kappa^2}{m^2} \left(\ln 8\kappa - \sum_{k=1}^m \frac{2}{2k-1} \pm \frac{a}{2\pi} \int_0^{2\pi} \int_0^{2\pi} d\phi_1 d\phi_2 \frac{\cos m\phi_1 \cos m\phi_2}{|\mathbf{y}_1(\phi_1) - \mathbf{y}_2(\phi_2)|} \right)^{-1} \quad (4.17)$$

along with a similar expression for $\mathcal{E}^{(m,s,\pm)}$ where $\cos m\phi_1 \cos m\phi_2$ is replaced by $\sin m\phi_1 \sin m\phi_2$. In Fig. 6, the dashed-dotted curves depict approximation (4.17) for $\mathcal{E}^{(1,c,+)}$ and $\mathcal{E}^{(1,s,+)}$. Despite the approximation being heuristic, the agreement with the semianalytical slender-body scheme (4.16) is reasonably good for all d/a and especially at moderately large d/a . It is clear that this approximation is exact for $d = 0$ and asymptotically correct as $d/a \rightarrow \infty$.

3. Noncoaxial heterodimers

Consider now a bilayer heterodimer where the torus-shaped rings are not identical. Unlike in the bilayer homodimer scenario considered above, now the spectrum of Fourier harmonics comprising each mode undergoes significant evolution as the horizontal displacement d is increased from the coaxial case $d = 0$ or, alternatively, decreased from the isolated-ring case $d = \infty$. Moreover, we find that this

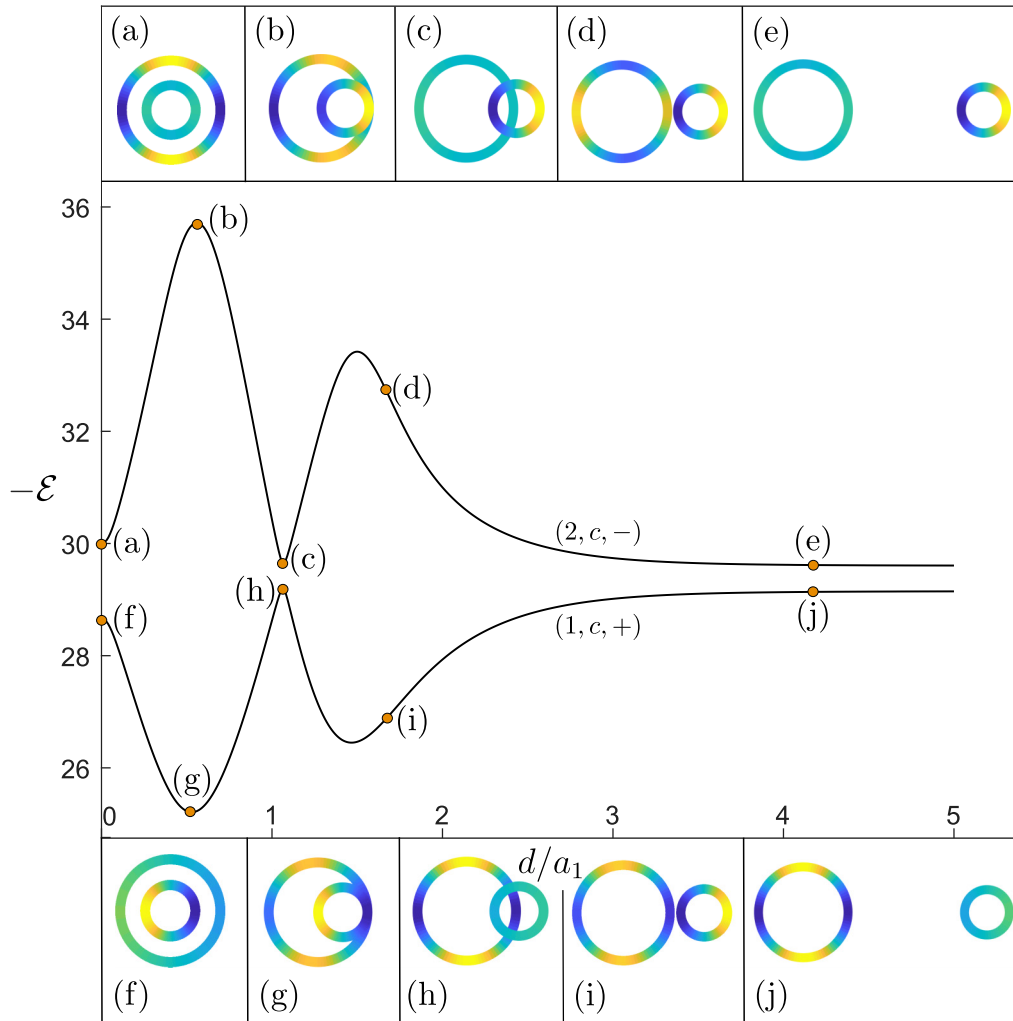


FIG. 7. Evolution as a function of d/a_1 of two eigenvalues of the bilayer heterodimer configuration schematically shown in Fig. 4, in the case $\kappa_1 = 10$, $\kappa_2 = 5$, $a_1/a_2 = 2$, and $h/a_1 = 0.3$. The modes are those continued from the in-phase dipolar mode $(1, c, +)$ and out-of-phase quadrupolar mode $(2, c, -)$, respectively, of the coaxial configuration obtained for $d = 0$. Also shown are the voltage eigenfunctions at the indicated values of d/a_1 .

evolution can continuously link two different Fourier harmonics in the latter limiting cases, in which each mode is composed of a single Fourier harmonic. We demonstrate this in Fig. 7 by considering the evolution of the two modes continued from the coaxial in-phase dipolar mode $(1, c, +)$ and out-of-phase quadrupolar mode $(2, c, -)$, respectively, with the geometric parameters of the two rings chosen such that the eigenvalues are close in the coaxial configuration. In the coaxial configuration, the mode $(2, c, -)$ is dominated by a quadrupolar distribution in the larger ring, whereas the mode $(1, c, +)$ is dominated by a dipolar distribution in the smaller ring. As d is continuously increased to ∞ , the mode $(2, c, -)$ is ultimately dominated by the dipolar mode $(1, c)$ of the smaller ring; similarly, the mode $(1, c, +)$ is ultimately dominated by the quadrupolar mode $(2, c)$ of the larger ring. This evolution is seen to involve multiple stages during which the Fourier harmonics of each mode undergo mixing and the eigenvalues split apart and then reapproach each other twice. We will see in Sec. VI some of the implications of this evolution in the context of the scattering problem.

V. FURTHER GEOMETRIC EXTENSIONS

A. Arbitrary cross-sectional shapes

It is straightforward to extend our theoretical framework to allow for noncircular cross-sectional shapes. In particular, let us briefly revisit the derivation in Sec. III B of the single-ring reduced eigenvalue problem. Given our focus on longitudinal modes of slender rings, we still expect that the interior potential is approximately uniform over the ring's cross section and varies mainly in the azimuthal direction. Thus, the representation (3.1) of the interior potential by an azimuthal voltage profile still holds. The exterior potential in the vicinity of the ring, however, can no longer be approximated as in (3.4) since that radially symmetric distribution assumes that the cross sections are circular. Nonetheless, it can be shown that (3.4) still holds at intermediate radial distances from the centerline, i.e., $b \ll r \ll a$, if only the cross-sectional radius $bf(\phi)$ is replaced by the so-called ‘‘conformal radius,’’ say $bf^*(\phi)$, of the cross-sectional geometry at the azimuthal angle ϕ . Working in the corresponding cross-sectional plane, the conformal radius

$bf^*(\phi)$ can be extracted from a conformal mapping from the exterior of a circle of that radius to the domain exterior to the true cross section (see, e.g., [38, Chap. 5] and [63]). In particular, for elliptical cross sections with semidiameters $b\sigma_1(\phi)$ and $b\sigma_2(\phi)$, one finds $bf^*(\phi) = (b\sigma_1(\phi) + b\sigma_2(\phi))/2$. Expressions for several other geometries can be found in [64, Table 1]. As a consequence, $f(\phi)$ should be replaced by $f^*(\phi)$ in the capacitance relation (3.9), while (3.7) remains

$$\mathcal{E}^{(m)} = -\frac{2\pi\kappa^2}{m^2\bar{A}} \left(\ln \frac{8\kappa}{f^*} - 2 \sum_{k=1}^m \frac{1}{2k-1} \right)^{-1} \quad \text{for } m = 1, 2, \dots \quad (5.1)$$

Note the logarithmically weak influence of the ring's cross-sectional shape, which we emphasize is a specific feature of the longitudinal modes considered herein. This prediction is consistent with the experimental and numerical results in [65], which show only slight differences between the plasmon-resonance frequencies of rings of different cross-sectional shape yet similar cross-sectional area.

B. Chain of rings

For clarity of exposition, we have so far considered either single rings or ring dimers. It is straightforward, however, to extend our approximation scheme to a system consisting of an arbitrary number of interacting rings. In particular, here we consider a coaxial chain of N not necessarily identical azimuthally invariant rings. (In light of the preceding generalization, azimuthally invariant does not necessarily imply torus shaped.) In this case, the appropriate reduced eigenvalue problem can be treated analytically. The analysis closely follows the derivation in Sec. IV B for a coaxial dimer of torus-shaped rings. Similar to the latter case, symmetry implies collective modes, with azimuthal number $m = 1, 2, \dots$, in which the voltage eigenfunction in the n th ring is $v_n = c_n \cos m\phi$. (There are also $\pi/2$ rotations of these collective modes having the same eigenvalues.) Following the steps in Sec. IV B, for given m we find the $N \times N$ generalized matrix-eigenvalue problem [cf. (4.11)]

$$\mathbf{c} = -\mathcal{E} \mathbf{G} \cdot \mathbf{c}, \quad (5.2)$$

where $\mathbf{c} = (c_1, c_2, \dots, c_N)^T$ and \mathbf{G} is an m -dependent $N \times N$ matrix whose components are defined analogously to (4.12).

As an example, we employ (5.2) to calculate the eigenfunctions of a finite coaxial chain of torus-shaped rings. Specifically, we consider a chain consisting of a series of identical, equally spaced, homodimers, where the center dimer is replaced by a homotrimer. In Fig. 8, we focus our attention on the dipolar modes of the chain ($m = 1$), for which the permittivity-eigenvalue spectrum is seen to consist of two disjoint, nearly continuous, bands formed of a large number of densely distributed eigenvalues; the lower- and higher-energy bands, respectively, cross the eigenvalues $\mathcal{E}^{(1,-)}$ and $\mathcal{E}^{(1,+)}$ of the dimers in isolation (Sec. IV B). Additionally, there are two isolated eigenvalues, one in the spectral gap between the two bands and one at an energy lower than the lower-energy band. As demonstrated in the figure, the isolated eigenvalues

unchanged, with $\bar{A}(\phi)$ still denoting the scaled cross-sectional area $A(\phi)/b^2$. The significance of the present extension is that, in contrast to the case of circular cross sections, $\bar{A}(\phi)$ can now be tuned independently from $f^*(\phi)$. The generalization of this extension to the case of ring dimers is evident.

Consider, for example, an azimuthally uniform ring whose cross-sectional shape is arbitrary. The eigenvalues follow from the result (3.17) for a torus-shaped ring as

correspond to modes that are localized around the defect. We remark that (5.2) predicts localized modes for all m , not only for the dipolar modes. In retrospect, the existence of localized modes rationalizes the application of our quasistatic theory to the case of an extended chain of rings, whose total length in any realistic scenario would be at least comparable to the free-space wavelength. Accordingly, we expect nonlocalized modes of the chain to be significantly affected by retardation [66].

VI. PLANE-WAVE ILLUMINATION

Armed with our slender-body approximations for the longitudinal modes of slender-ring structures, we return to the quasistatic scattering problem formulated in Sec. II A. There, the near-field potential $\varphi(\mathbf{x})$ generically possesses the asymptotic far-field behavior [67]

$$\varphi(\mathbf{x}) \sim -\mathbf{E}_\infty \cdot \mathbf{x} + \mathbf{E}_\infty \cdot \boldsymbol{\alpha} \cdot \frac{\mathbf{x}}{4\pi|\mathbf{x}|^3} \quad \text{as } |\mathbf{x}| \rightarrow \infty, \quad (6.1)$$

in which $\boldsymbol{\alpha}$ is the polarizability tensor of the structure. In terms of that tensor, quasistatic approximations for the extinction and absorption cross sections in the direction of the applied field, say $\hat{\mathbf{i}}$, are given by [35]

$$C_{\text{ext}}, C_{\text{abs}} = \frac{2\pi}{\lambda} \hat{\mathbf{i}} \cdot \text{Im} \boldsymbol{\alpha}, \quad (6.2)$$

where λ denotes the wavelength of the incident plane wave. We shall use the approximation scheme developed in this paper to calculate $\boldsymbol{\alpha}$ and hence C_{abs} for a range of slender-ring geometries.

A slender-body approximation for $\boldsymbol{\alpha}$ can be extracted by considering the large- $|\mathbf{x}|$ expansion of the spectral solution (2.4) and substituting the slender-body approximations for the voltage eigenfunctions and eigenvalues. For a structure formed of N arbitrarily shaped rings, we find

$$\boldsymbol{\alpha} = \frac{1}{\epsilon_0} \sum_{l \in \mathcal{I}} \frac{\epsilon_r(\omega) - 1}{\epsilon_r(\omega) - \mathcal{E}^{(l)}} \times \frac{\left(\sum_{n=1}^N a_n \int_0^{2\pi} d\phi \mathbf{y}_n q_n^{(l)} \right) \left(\sum_{n=1}^N a_n \int_0^{2\pi} d\phi \mathbf{y}_n q_n^{(l)} \right)}{\sum_{n=1}^N a_n \int_0^{2\pi} d\phi q_n^{(l)} v_n^{(l)}}. \quad (6.3)$$

A derivation of this result is given in Appendix D. We note that it only includes the longitudinal modes studied in this paper,

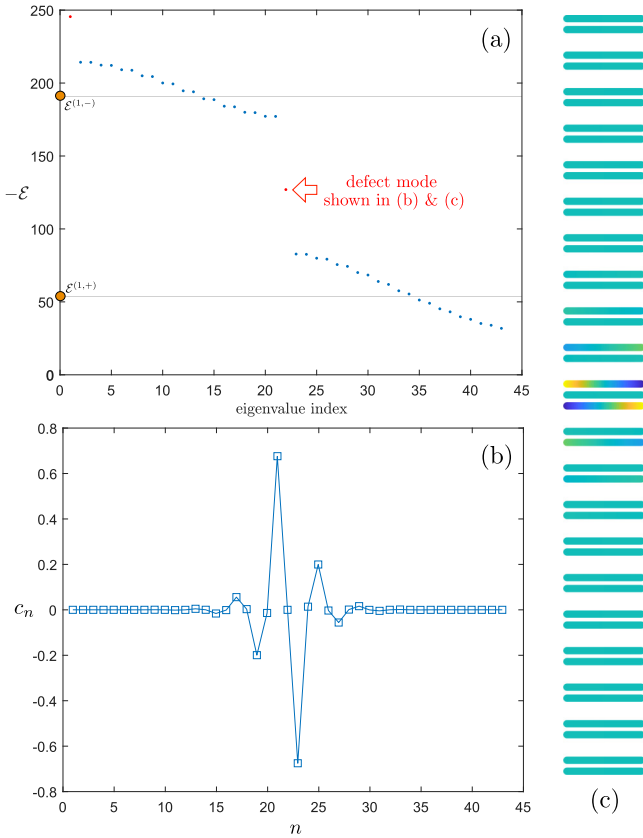


FIG. 8. (a) Eigenvalues of the “dipolar” ($m = 1$) modes of a coaxial chain of $N = 43$ identical torus-shaped rings ($\kappa = 10$). The chain consists of two identical subchains, each formed of 10 dimers (spacing between rings and dimers being 0.3 and 0.7 times the ring radius, respectively), which are linked by a trimer (spacings similar to dimer subchains). Each eigenvalue is doubly degenerate, corresponding to a $\pi/2$ rotation of the eigenfunctions about the symmetry axis. The spectrum is calculated in the slender-body approximation by solving (5.2). It consists of two nearly continuous bands that cross the eigenvalues $\mathcal{E}^{(1,\pm)}$ of the dimers in isolation. Additionally, there are two isolated eigenvalues which are associated with localized “defect modes.” The defect mode marked in (a) is visualized in terms of the dipole intensities c_n [cf. (5.2)] in (b) and voltage profiles in (c). The horizontal lines in (a) mark the eigenvalues $\mathcal{E}^{(1,-)}$ and $\mathcal{E}^{(1,+)}$ of the dimers in isolation.

which for low frequencies $\omega \ll \omega_p$ dominate the plasmonic response as further discussed in [39] and the concluding Sec. VIII.

To evaluate (6.3) for general ring geometries, we employ the semianalytical scheme (4.16), whose generalization from the case of two to N rings is straightforward; furthermore, noncircular cross sections can be included in that scheme as discussed in Sec. V A.

In the special cases of single azimuthally invariant rings, as well as azimuthally invariant coaxial dimers, it is possible to evaluate the integrals appearing in (6.3) in closed form. In those cases, symmetry dictates that the polarizability tensor possesses the form $\alpha = (\hat{\mathbf{e}}_x \hat{\mathbf{e}}_x + \hat{\mathbf{e}}_y \hat{\mathbf{e}}_y) \alpha$, where $\hat{\mathbf{e}}_x$ and $\hat{\mathbf{e}}_y$ are orthogonal unit vectors parallel to the plane defined by the rings and α is a scalar polarizability. Furthermore, each mode involves a single Fourier harmonic, and since the centerlines

\mathbf{y}_n are circular curves, the overlap integrals in the numerator of (6.3) vanish for all except the dipolar modes. Assuming for simplicity that the azimuthally invariant rings are torus shaped, we use the results of Sec. III to find

$$\alpha = \frac{\epsilon_r(\omega) - 1}{\epsilon_r(\omega) - \mathcal{E}^{(1)}} \frac{2\pi^2 a^3}{\ln 8\kappa - 2}, \quad (6.4)$$

with the slender-body approximation for $\mathcal{E}^{(1)}$ provided by (3.17). Similarly, using the results of Sec. IV B, we find for a coaxial dimer of torus-shaped rings

$$\alpha = \sum_{\pm} \frac{1 - \epsilon_r(\omega)}{\epsilon_r(\omega) - \mathcal{E}^{(1,\pm)}} \frac{\pi \mathcal{E}^{(1,\pm)} (A_1 c_1^{(1,\pm)} + A_2 c_2^{(1,\pm)})^2}{\frac{A_1}{a_1} (c_1^{(1,\pm)})^2 + \frac{A_2}{a_2} (c_2^{(1,\pm)})^2}, \quad (6.5)$$

with $c_1^{(1,\pm)}$ and $c_2^{(1,\pm)}$ provided by (4.14) and a slender-body approximation for $\mathcal{E}^{(1,\pm)}$ provided by (4.13). In the more specific coaxial homodimer case, the numerator in (6.5) vanishes identically for the out-of-phase dipolar mode, namely, because the induced dipole excited in the two rings cancels. Thus, (6.5) degenerates to

$$\alpha = \frac{\epsilon_r(\omega) - 1}{\epsilon_r(\omega) - \mathcal{E}^{(1,+)}} \frac{4\pi^2 a^3}{\ln 8\kappa - 2 + \frac{1}{2} \Delta_1}, \quad (6.6)$$

where $\mathcal{E}^{(1,+)}$ now possesses the slender-body approximation (4.8) and Δ_1 is given by (4.9).

In formulas (6.3)–(6.6), resonance of mode I is associated with cancellation in the denominator of the frequency-dependent factor $F^{(I)} = [\epsilon_r(\omega) - 1]/[\epsilon_r(\omega) - \mathcal{E}^{(I)}]$. Let $\mathcal{E}_0^{(I)}$ denote the slender-body approximation for $\mathcal{E}^{(I)}$. We stress that the approximation $F \approx [\epsilon_r(\omega) - 1]/[\epsilon_r(\omega) - \mathcal{E}_0^{(I)}]$ only holds if $|\mathcal{E}^{(I)} - \mathcal{E}_0^{(I)}| \ll \text{Im}[\epsilon_r(\omega)]$, namely, if the loss is large relative to the error in the slender-body approximation for the eigenvalue. On the one hand, the algebraic order of the latter error is smaller than κ^2 , though we do not know whether it is unity, κ , or some other scaling $\ll \kappa^2$. On the other hand, the Drude model (2.2) and eigenvalue scaling (3.12) together imply $\text{Im}[\epsilon_r(\omega)] \simeq \kappa^3 (\gamma/\omega_p)$, suggesting that the condition is easily met for the longitudinal resonances. This is confirmed by the comparison below with exact quasistatic solutions. Even if the condition $|\mathcal{E}^{(I)} - \mathcal{E}_0^{(I)}| \ll \text{Im}[\epsilon_r(\omega)]$ is not met, formulas (6.3)–(6.6) still give a valid approximation for the resonance curve only shifted in frequency; moreover, the approximation $F^{(I)} \approx \mathcal{E}_0^{(I)}/\text{Im}(\epsilon_r)$ still holds at resonance, i.e., at ω such that $\text{Im}(\epsilon_r) = \mathcal{E}^{(I)}$.

We now apply the above results for the scattering problem to several ring structures whose plasmonic eigenvalues and eigenfunctions we have analyzed earlier in the paper. In particular, we consider single torus-shaped and azimuthally nonuniform rings, as well as coaxial and noncoaxial dimers of torus-shaped rings. In Fig. 9, we show C_{abs} , normalized by the planar area πa^2 , for a torus-shaped ring alongside that for the azimuthally nonuniform ring from Fig. 3. The incident-field direction $\hat{\mathbf{t}}$ is parallel to the plane of the ring; in the case of the azimuthally nonuniform ring, $\hat{\mathbf{t}}$ is further specified as pointing towards the direction of maximum thickness of the ring. For the torus-shaped ring, the slender-body approximation (6.4) is compared with the exact quasistatic computations in [68] and good agreement is found despite the aspect ratio $\kappa = 10$ being

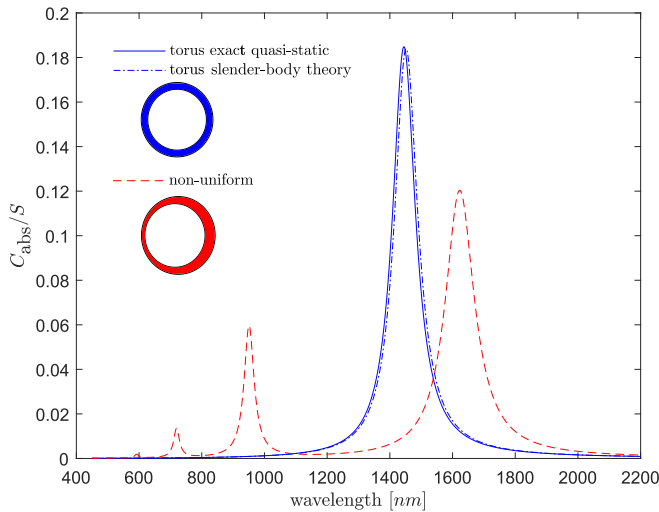


FIG. 9. Absorption cross section (6.2), normalized by $S = \pi a^2$, for the torus-shaped and azimuthally nonuniform rings defined in the caption of Fig. 3. The incident-field direction $\hat{\mathbf{i}}$ is in the plane of the ring, pointing in the maximum-thickness direction in the case of the azimuthally nonuniform ring. For the torus-shaped ring, the slender-body approximation (6.4) is compared with an exact quasistatic solution [68]. The slender-body approximation for the azimuthally nonuniform ring is evaluated numerically from (6.3). We assume the Drude model (2.2) with $\omega_p = 1.196 \times 10^{16}$ rad/s and $\gamma = 8.05 \times 10^{13}$ rad/s.

only moderately large. The torus-shaped ring exhibits a single resonance peak, which is associated with the excitation of the cosine-dipolar mode (1, c) shown at the top-right corner of Fig. 3. (With ϕ measured from $\hat{\mathbf{i}}$, the corresponding sine mode is not excited.) In contrast, for the azimuthally nonuniform ring, we observe multiple resonance peaks. As explained in Sec. III D 3, in that case all modes generally include a dipolar component (first Fourier harmonic). Accordingly, the overlap integrals in (6.3) do not vanish identically as they do in the torus case for $m > 1$. In particular, the lowest- and second-lowest-frequency peaks seen in Fig. 9 are due to excitation of the “dipolar” mode (1, c) and “quadrupolar” mode (2, c) shown on the left of Fig. 3.

In Fig. 10, we show C_{abs} , normalized by the planar area πa_1^2 , for several bilayer dimer configurations formed of torus-shaped rings: a coaxial homodimer (same as in Fig. 5), a coaxial heterodimer (same as in Figs. 5 and 7 for $d = 0$), and a bilayer noncoaxial heterodimer (same as in Fig. 7 for $d/a_1 = 0.5$). The incident-field direction $\hat{\mathbf{i}}$ is taken parallel to the planes of the rings; in the noncoaxial-heterodimer case, $\hat{\mathbf{i}}$ is further specified as pointing along the direction of the horizontal displacement of the smaller ring.

For the coaxial homodimer, we observe a single resonant peak, a prediction which is clearly inferred from the closed-form slender-body approximation (6.6). This is because only the in-phase cosine-dipolar mode (1, c , +) is excited by the plane wave. (With ϕ measured from $\hat{\mathbf{i}}$, the corresponding sine mode is not excited.) While this is not demonstrated here, we know from the analytical expression (4.8) for $\mathcal{E}^{(1,+)}$, or from Fig. 5(a), to expect this peak to blueshift with decreasing distance between the rings. This is opposite to the trend ob-

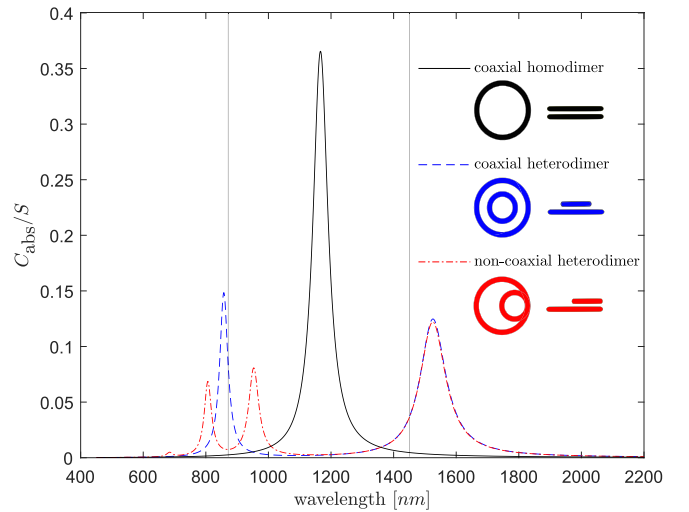


FIG. 10. Absorption cross section (6.2), normalized by $S = \pi a_1^2$, for the coaxial homodimer of Fig. 5; the coaxial heterodimer of Figs. 5 and 7 for $d = 0$; and the bilayer heterodimer of Fig. 7 for $d/a_1 = 0.5$. In all cases $a_1 \geq a_2$ and the incident-field direction $\hat{\mathbf{i}}$ is in the plane of the rings, pointing in the direction of the horizontal displacement of the smaller ring in the noncoaxial case. The curves represent slender-body approximations evaluated using (6.6) for the coaxial homodimer, (6.5) for the coaxial heterodimer, and (6.3) for the noncoaxial heterodimer. The vertical lines mark the frequencies corresponding to the eigenvalues $\mathcal{E}^{(1)}$ of the larger and smaller torus-shaped rings in isolation. We assume the Drude model (2.2) with $\omega_p = 1.196 \times 10^{16}$ rad/s and $\gamma = 8.05 \times 10^{13}$ rad/s.

served for the analogous low-frequency bonding-gap modes of sphere dimers [11, 15, 17, 20].

For the coaxial heterodimer, we observe an additional resonance peak at higher frequency. This is because the net dipole induced in the rings for the out-of-phase dipolar modes does not cancel out between the two rings as it does in the coaxial-homodimer case. This feature is easily inferred from the slender-body approximation (6.5), which explicitly shows two resonances associated with the in-phase and out-of-phase dipolar modes. (With ϕ measured from $\hat{\mathbf{i}}$, it is again only the “cosine” dipolar modes that are excited.) As seen in Fig. 5(b), for this configuration the out-of-phase dipolar mode is dominated by a dipolar distribution in the larger ring, whereas the in-phase dipolar mode is dominated by a dipolar distribution in the smaller ring. From Fig. 5(a), we expect the in-phase and out-of-phase resonance to, respectively, blueshift and redshift as the vertical distance between the rings is reduced.

Consider next the noncoaxial-heterodimer configuration. Similarly to the azimuthally nonuniform ring, we observe multiple resonance peaks owing to the absence of axial symmetry. In particular, we note that the higher-frequency resonance in the coaxial-heterodimer case, which is associated with the in-phase-dipolar mode (1, c , +) of that configuration, is replaced by two distinct peaks. This can be understood from the study carried out in Fig. 7. Thus, this pair of resonances are associated with the excitation of the two modes continued from the in-phase-dipolar (1, c , +) and out-of-phase-quadrupolar (2, c , -) modes of the corresponding coaxial-heterodimer configuration. While, owing to symmetry, in the coaxial case only dipolar modes are excited,

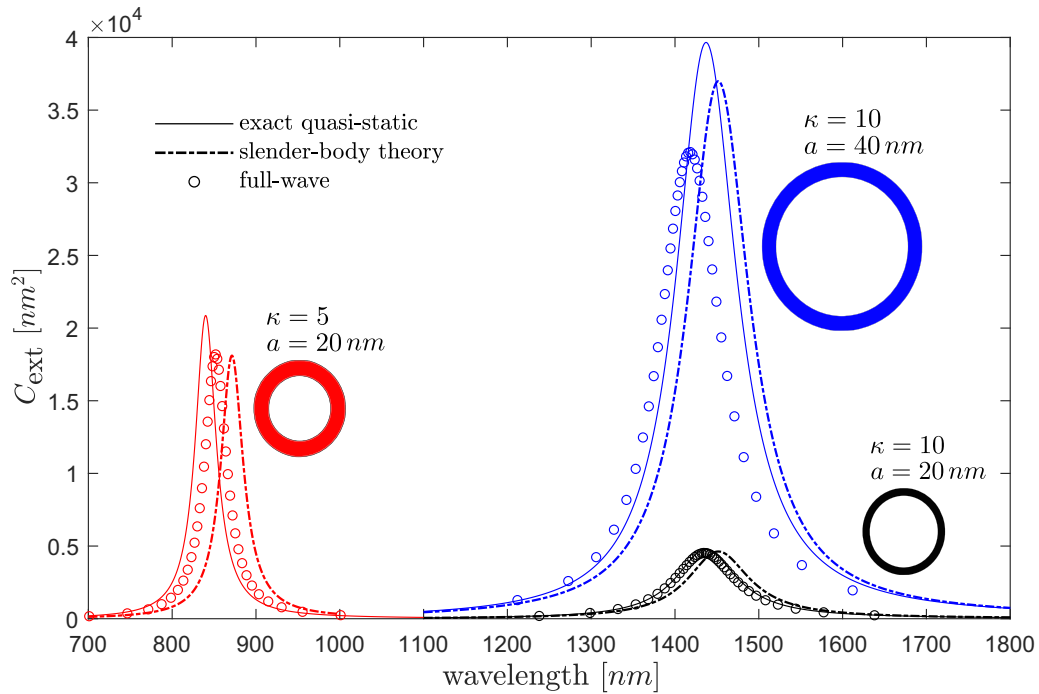


FIG. 11. Extinction cross section for torus-shaped rings for the indicated values of the ring radius a and aspect ratio κ . The incident field is parallel to the ring plane. Solid lines: solutions exact in the quasistatic approximation [68]. Dashed-dotted lines: slender-body approximation (6.4). Circles: full-wave numerical computations using the MNPBEM toolbox [71]. We assume the Drude model (2.2) with $\omega_p = 1.196 \times 10^{16}$ rad/s and $\gamma = 8.05 \times 10^{13}$ rad/s.

in the noncoaxial case both modes include dipolar components and can therefore be excited. Specifically, the noncoaxial configuration is as shown in Figs. 7(b) and 7(g), in which case the eigenvalues are farthest apart as a function of the horizontal displacement, and both modes have a visible dipolar component in the smaller ring.

VII. VALIDITY OF QUASISTATIC FORMULATION

The theory in this paper is predicated on the quasistatic approximation, which is widely used to describe the localized-surface-plasmon resonances of nanometallic structures [2]. In this approximation, radiation damping is neglected on the basis of the smallness of the particle relative to the free-space wavelength, and the near field of the particle is assumed to be irrotational and forced by the field locally associated with the incident radiation. For sufficiently weak material loss, however, radiative corrections must in fact be appreciable even for particles which are much smaller than the free-space wavelength [69,70]. In the concluding Sec. VIII, we discuss opportunities to extend the present theory to incorporate radiative corrections for low-loss subwavelength particles, as well as to a full-wave theory for slender rings whose diameter is comparable to the free-space wavelength. Here, we derive a scaling condition for the quasistatic formulation to adequately describe the longitudinal resonances of a slender ring. Furthermore, we illustrate these constraints by comparing with full-wave simulations. Consider first the condition for a slender ring to be subwavelength at its longitudinal resonances. At the level of scalings, and ignoring logarithmic factors, (2.2) and (3.12) give the free-space wavelength $\lambda \simeq \kappa \lambda_p$,

where $\lambda_p = 2\pi c/\omega_p$. Thus, the condition $a \ll \lambda$ implies $a \ll \lambda_p \kappa$ or, for the typical value $\omega_p = 1.196 \times 10^{16}$ rad/s, $a \ll \kappa \times 150$ nm. Under this condition, which is met even for quite large slender rings, the field is approximately irrotational in the vicinity of the ring, whereby the quasistatic modes remain relevant to the expansion of that near field. Nonetheless, the quasistatic scattering problem formulated in Sec. II, and in particular its spectral solution (2.4), is valid under a more stringent condition. Thus, the scattering cross section, which scales like $k^4 \alpha^2$ in the quasistatic approximation, must be negligible compared to the absorption cross section. Using (6.2), this implies $\alpha \ll \lambda^3$. Estimating λ at the longitudinal resonances as before, and using (6.4) [with (3.12)], we find $a^3/\text{Im}(\epsilon_r) \ll \kappa \lambda_p^3$. More explicitly, using the Drude model (2.2) to estimate $\text{Im}(\epsilon_r)$ [with (3.12)] we can write this condition as

$$\frac{a}{\lambda_p} \ll \left(\frac{\gamma}{\omega_p} \right)^{1/3} \times \kappa^{4/3}. \quad (7.1)$$

For typical parameters (same ω_p as above and $\gamma = 8.05 \times 10^{13}$ rad/s), we have $a \ll \kappa^{4/3} \times 30$ nm.

In Fig. 11, we show a comparison between quasistatic and full-wave predictions for the extinction cross section of a torus-shaped ring ($\kappa = 10$, typical values of ω_p and γ as above), with the incident field in the ring plane. The full-wave results are obtained by boundary-element simulation using the the MNPBEM toolbox [71]. As for the quasistatic results, both exact [68] and slender-body approximations are shown [cf. (6.4)]. This comparison demonstrates the improved agreement between full-wave and quasistatic predictions with decreasing a and increasing κ .

VIII. CONCLUDING REMARKS

We have developed an approximate theory to describe the longitudinal localized-surface-plasmon resonances of slender metallic nanorings of virtually arbitrary shape, as well as more involved nanometallic structures formed of two or more such rings, the separation between the rings being comparable with their centerline radii. At the heart of the theory is an asymptotic reduction of the 3D plasmonic eigenvalue problem governing the material- and frequency-independent longitudinal modes of the structure to a reduced 1D formulation, in which the plasmonic eigenmodes are represented by azimuthal voltage and polarization-charge profiles attached to each ring. Once this reduced eigenvalue problem has been solved for a given geometry, approximations for the near-field eigenfunctions in 3D can be extracted from their associated 1D eigenfunctions. When joined with the standard spectral theory of plasmonic resonance, this provides the means to obtain any quantity of interest in a physical scattering problem (that involves the same geometry), such as scattering cross sections. Overall, the present theoretical framework allows to rapidly gauge the plasmonic properties of unprecedentedly complex 3D structures, which may foster the study of new plasmonic structures and phenomena.

Our approximation approach heavily draws on a transfer of knowledge from the field of fluid dynamics, where approximations of the sort derived here are known as slender-body theory. We stress that the slender-body theory developed herein is of the more accurate “nonlocal” type, which in the present context means that we account for electrostatic interactions between any two azimuthal segments of any of the rings forming the structure. The inclusion of these interactions can be shown to ensure an “algebraic” rather than “logarithmic” asymptotic accuracy of the scheme in the large-aspect-ratio limit pertinent to slender rings. This claimed accuracy is demonstrated by the good agreement in Figs. 2 and 9 with known solutions for single torus-shaped rings.

To demonstrate the versatility of the theory, we have applied it to the calculation of the longitudinal modes and absorption cross sections of a number of configurations. Still, it is clear that we only considered a small sample of the wide range of geometries that can be studied. For several families of geometries, namely, azimuthally invariant rings (not necessarily torus shaped) and coaxial dimers and chains thereof, the reduced formulation was solved in closed form, thus generating several apparently new analytical approximations. We also considered a range of other geometries, including azimuthally nonuniform rings and noncoaxial multiple-ring configurations. In the latter cases, we solved the reduced formulation using straightforward semianalytical schemes, in which the 1D eigenfunctions are represented by their Fourier coefficients.

We have focused on the description of the longitudinal (low-frequency) modes of slender-ring structures, as defined in the Introduction and in Sec. III B, as well as the excitation of these modes by incident plane waves. Slender rings also possess nonlongitudinal, or transverse modes, characterized by polarization-charge distributions which, in contrast to the longitudinal case, exhibit significant variation in the cross-sectional planes. As we discussed in [39], and others have observed in theory and experiments [72,73], the contribu-

tion of nonlongitudinal modes to the resonant response of slender bodies is generally negligible, except in specialized excitation scenarios involving near-field sources located very close to the structure. To treat those cases, our slender-body theory could be extended to describe the transverse modes of slender-ring structures. A leading-order analysis, as done in [39] for axisymmetric bodies, shows that those modes essentially correspond to the in-plane modes of an infinite cylinder, hence with the permittivity eigenvalues satisfying the asymptotic behavior $\mathcal{E} \rightarrow -1$ as $\kappa \rightarrow \infty$. [Alluding to Drude’s model (2.2), we see that transverse modes are high frequency relative to longitudinal modes.] To consider corrections to this leading behavior, one would need to match the dipolar (or quadrupole, etc.) cross-sectional potential distributions with an approximation of the potential on the ring scale formed by superposition of the corresponding potential singularities along the centerline of the body.

Another desirable extension to this work would be to consider the effects of retardation and radiation damping. In particular, there exists a generalization of the spectral approach employed herein based on permittivity eigenvalues to the full-wave regime [74–77]. In that generalized formulation, the permittivity eigenvalues become complex valued and frequency dependent. To describe the regime of low-loss and moderately subwavelength slender-ring structures, where deviations from the quasistatic can be substantial (as demonstrated in Sec. VII), it would be necessary to carry out a low-frequency analysis of the generalized eigenvalue problem up to the order of the permittivity eigenvalue that is comparable to the imaginary part of the physical permittivity. (This regime could also be described by applying suitable corrections to the quasistatic predictions following [69,78–80].) Another avenue would be to develop a full-wave slender-body theory in the case where the ring diameter is comparable to the free-space wavelength; the cross-sectional scale would still be subwavelength, while the ring-scale approximation could be formed by superposition of fundamental solutions of Maxwell’s equations along the centerline of the ring. Lastly, we note that it is possible but not straightforward to generalize the permittivity-eigenvalue formulation to multiconstituent photonic structures [81], e.g., hybrid metal-dielectric structures. For such ring structures, a reformulation of the theory based on quasinormal modes and complex frequency eigenvalues may be more convenient [82].

ACKNOWLEDGMENT

The authors acknowledge funding from EPSRC UK (New Investigator Award EP/R041458/1).

APPENDIX A: MATCHING THE RING AND CROSS-SECTIONAL SCALES

In this Appendix, we shall derive the small- r behavior of the ring-scale potential (3.8). A preliminary step is to write that solution in the form

$$\begin{aligned} \phi = & \frac{q(\phi)}{4\pi\epsilon_0} \int_0^{2\pi} a d\phi' \frac{1}{|\mathbf{x}(r, \theta, \phi) - \mathbf{y}(\phi')|} \\ & + \frac{1}{4\pi\epsilon_0} \int_0^{2\pi} a d\phi' \frac{q(\phi') - q(\phi)}{|\mathbf{x}(r, \theta, \phi) - \mathbf{y}(\phi')|}, \end{aligned} \quad (\text{A1})$$

where the geometry gives

$$|\mathbf{x}(r, \theta, \phi) - \mathbf{y}(\phi')| = \sqrt{r^2 + 4(a^2 + ar \cos \theta) \sin^2 \frac{\phi - \phi'}{2}}. \quad (\text{A2})$$

Using (A2), it is readily seen that the second integral in (A1) is regular as $r \rightarrow 0$:

$$\begin{aligned} & \int_0^{2\pi} a d\phi' \frac{q(\phi') - q(\phi)}{|\mathbf{x}(r, \theta, \phi) - \mathbf{y}(\phi')|} \\ &= \int_0^{2\pi} d\phi' \frac{q(\phi') - q(\phi)}{2 \sin \frac{|\phi - \phi'|}{2}} + o(1) \quad \text{as } r \rightarrow 0. \end{aligned} \quad (\text{A3})$$

To treat the first integral in (A1), which is singular as $r \rightarrow 0$, we use the method of splitting the range of integration [38]. Thus, we write

$$\begin{aligned} & \int_0^{2\pi} a d\phi' \frac{1}{|\mathbf{x}(r, \theta, \phi) - \mathbf{y}(\phi')|} \\ &= \left\{ \int_0^\delta dt + \int_\delta^\pi dt \right\} \frac{2}{\sqrt{\bar{r}^2 + 4(1 + \bar{r} \cos \theta) \sin^2 \frac{t}{2}}}, \end{aligned} \quad (\text{A4})$$

where we introduce the normalized radial coordinate $\bar{r} = r/a$ and an auxiliary parameter in the range $\bar{r} \ll \delta \ll 1$. Denote the first integral on the right-hand side of (A4) by I_1 . Making the change of variables $\tau = t/\bar{r}$, we have

$$I_1 = 2 \int_0^{\delta/\bar{r}} \frac{d\tau}{\sqrt{1 + 4(1 + \bar{r} \cos \theta) \bar{r}^{-2} \sin^2(\bar{r}\tau/2)}}. \quad (\text{A5})$$

Using $\bar{r}\tau < \delta \ll 1$, the integrand can be expanded to show that

$$\begin{aligned} I_1 &= 2 \int_0^{\delta/\bar{r}} \frac{d\tau}{(1 + \tau^2)^{1/2}} + o(1) \\ &= 2 \ln \frac{2\delta}{\bar{r}} + o(1) \quad \text{as } \bar{r} \rightarrow 0, \end{aligned} \quad (\text{A6})$$

where for the last step we used $\delta/\bar{r} \gg 1$. Similarly, denote the second integral on the right-hand side of (A4) by I_2 . Using $t > \delta \gg \bar{r}$, the integrand of that integral can be expanded to

$$\mathcal{N}[\cos m\phi] = 2\mathcal{N}\{\cos[(m-1)\phi] \cos \phi\} - \lambda_{m-2} \cos[(m-2)\phi]. \quad (\text{B5})$$

Using (B1) and the first equation in (B2) for $n = m - 1$, we have

$$\begin{aligned} \mathcal{N}\{\cos[(m-1)\phi] \cos \phi\} &= \int_0^{2\pi} d\phi' \frac{\cos[(m-1)\phi'] \cos \phi' - \cos[(m-1)\phi] \cos \phi}{2 \sin \frac{|\phi' - \phi|}{2}} \\ &= \int_0^{2\pi} d\phi' \frac{\cos[(m-1)\phi'](\cos \phi' - \cos \phi)}{2 \sin \frac{|\phi' - \phi|}{2}} + \cos \phi \mathcal{N}\{\cos[(m-1)\phi]\} \\ &= - \int_0^{2\pi} d\phi' \frac{\cos[(m-1)\phi'] \sin \frac{\phi' - \phi}{2} \sin \frac{\phi' + \phi}{2}}{\sin \frac{|\phi' - \phi|}{2}} + \lambda_{m-1} \cos \phi \cos[(m-1)\phi] \\ &= 2 \frac{\cos[(m-2)\phi]}{2m-3} - 2 \frac{\cos m\phi}{2m-1} + \frac{1}{2} \lambda_{m-1} \{\cos m\phi + \cos[(m-2)\phi]\}. \end{aligned} \quad (\text{B6})$$

show that

$$I_2 = \int_\delta^\pi \frac{dt}{\sin \frac{t}{2}} + o(1) = 2 \ln \frac{4}{\delta} + o(1) \quad \text{as } \bar{r} \rightarrow 0. \quad (\text{A7})$$

Combining (A3), (A6), and (A7), we find the requisite behavior

$$\begin{aligned} \varphi(\mathbf{x}) &= \frac{q(\phi)}{2\pi\epsilon_0} \ln \frac{8a}{r} + \frac{1}{4\pi\epsilon_0} \int_0^{2\pi} d\phi' \frac{q(\phi') - q(\phi)}{2 \sin \frac{|\phi - \phi'|}{2}} \\ &+ o(1) \quad \text{as } r \rightarrow 0. \end{aligned} \quad (\text{A8})$$

APPENDIX B: PROOF OF IDENTITY (3.15)

In this Appendix we prove identity (3.15), which constitutes a diagonalization of the integral operator appearing in the capacitance relation (3.9). To this end, it is convenient to denote that integral operator as

$$\mathcal{N}[q(\phi)] = \int_0^{2\pi} d\phi' \frac{q(\phi') - q(\phi)}{2 \sin \frac{|\phi - \phi'|}{2}}. \quad (\text{B1})$$

We shall show that, for any non-negative integer n , there exists a constant λ_n such that

$$\mathcal{N}[\cos n\phi] = \lambda_n \cos n\phi, \quad \mathcal{N}[\sin n\phi] = \lambda_n \sin n\phi. \quad (\text{B2a,b})$$

Our method of proof will also furnish the constants, which constitute the eigenvalues of the operator \mathcal{N} . In what follows, we consider only the cosine eigenfunctions, the corresponding result for the sine eigenfunctions readily following from a straightforward change of variables.

Direct calculation shows that $\mathcal{N}[1] = 0$ and $\mathcal{N}[\cos \phi] = -4 \cos \phi$, hence that (B2a) holds for $n = 0$ and 1 with $\lambda_0 = 0$ and $\lambda_1 = -4$. Now, let m be any integer > 1 and assume that (B2a) also holds for $n = 1, \dots, m-1$, with

$$\lambda_n = -\frac{4}{2n-1} + \lambda_{n-1}. \quad (\text{B3})$$

This assumed difference relation is consistent with the result for $n = 1$ and implies that

$$\lambda_n = -4 \sum_{k=1}^n \frac{1}{2k-1} \quad \text{for } n = 1, \dots, m-1. \quad (\text{B4})$$

Next, we use the definitions (B1) and the first equation in (B2) for $n = m - 2$ to write

So, combining (B5) and (B6) gives

$$\mathcal{N}[\cos m\phi] = \left(\lambda_{m-1} - \frac{4}{2m-1} \right) \cos m\phi + \left(\lambda_{m-1} - \lambda_{m-2} + \frac{4}{2m-3} \right) \cos[(m-2)\phi], \quad (\text{B7})$$

where the second term on the right-hand side vanishes owing to (B3), while the first term on the right-hand side shows that (B3), and hence (B4), hold also for $n = m$. It follows by induction that (B2) holds for any non-negative integer n , with $\lambda_0 = 0$ and λ_n given by (B4) for $n > 0$.

APPENDIX C: SEMIANALYTICAL SCHEME

1. Single ring

For a single ring of nonuniform thickness, the reduced eigenvalue problem of Sec. III B is approximated by the generalized matrix-eigenvalue problem (3.21). In that problem, $\mathbf{M} = \{M_{n,k}\}$ and $\mathbf{U} = \{U_{n,k}\}$ are $2K \times 2K$ matrices with components

$$M_{n,k} = \frac{nk}{\pi} \times \begin{cases} \int_0^{2\pi} d\phi \bar{A}(\phi) \sin n\phi \sin k\phi, & n \leq K, k \leq K \\ -\int_0^{2\pi} d\phi \bar{A}(\phi) \sin n\phi \cos k\phi, & n \leq K, k > K \\ -\int_0^{2\pi} d\phi \bar{A}(\phi) \cos n\phi \sin k\phi, & n > K, k \leq K \\ \int_0^{2\pi} d\phi \bar{A}(\phi) \cos n\phi \cos k\phi, & n > K, k > K \end{cases} \quad (\text{C1})$$

and

$$U_{n,k} = -\frac{1}{\pi} \delta_{n,k} \sum_{k=1}^n \frac{1}{2k-1} + \frac{1}{2\pi^2} \times \begin{cases} \int_0^{2\pi} d\phi \cos n\phi \cos k\phi \ln \frac{8\kappa}{f(\phi)}, & n \leq K, k \leq K \\ \int_0^{2\pi} d\phi \cos n\phi \sin k\phi \ln \frac{8\kappa}{f(\phi)}, & n \leq K, k > K \\ \int_0^{2\pi} d\phi \sin n\phi \cos k\phi \ln \frac{8\kappa}{f(\phi)}, & n > K, k \leq K \\ \int_0^{2\pi} d\phi \sin n\phi \sin k\phi \ln \frac{8\kappa}{f(\phi)}, & n > K, k > K. \end{cases} \quad (\text{C2})$$

Furthermore, the coefficient α_0 can be calculated *a posteriori* as

$$\alpha_0 = \frac{1}{4\pi^2} \sum_{k=1}^K \int_0^{2\pi} d\phi (\tilde{\alpha}_k \cos k\phi + \tilde{\beta}_k \sin k\phi) \ln \frac{8\kappa}{f(\phi)}. \quad (\text{C3})$$

2. Ring dimer

For an arbitrary ring dimer, the generalized eigenvalue problem of Sec. IV A is approximated by the generalized matrix-eigenvalue problem (4.16). In that problem, the $2K \times 2K$ matrices \mathbf{M}_n and \mathbf{U}_n are like above with $n = 1, 2$ indicated the ring number, whereas $\mathbf{V} = \{V_{n,k}\}$ is a $2K \times 2K$ coupling matrix with components

$$V_{n,k} = \frac{\sqrt{a_1 a_2}}{4\pi^2} \begin{cases} \int_0^{2\pi} \int_0^{2\pi} d\phi_1 d\phi_2 \frac{\cos n\phi_1 \cos k\phi_2}{|y_1(\phi_1) - y_2(\phi_2)|}, & n \leq K, k \leq K \\ \int_0^{2\pi} \int_0^{2\pi} d\phi_1 d\phi_2 \frac{\cos n\phi_1 \sin k\phi_2}{|y_1(\phi_1) - y_2(\phi_2)|}, & n \leq K, k > K \\ \int_0^{2\pi} \int_0^{2\pi} d\phi_1 d\phi_2 \frac{\sin n\phi_1 \cos k\phi_2}{|y_1(\phi_1) - y_2(\phi_2)|}, & n > K, k \leq K \\ \int_0^{2\pi} \int_0^{2\pi} d\phi_1 d\phi_2 \frac{\sin n\phi_1 \sin k\phi_2}{|y_1(\phi_1) - y_2(\phi_2)|}, & n > K, k > K. \end{cases} \quad (\text{C4})$$

APPENDIX D: FAR-FIELD EXPANSION

In this Appendix we derive the far-field behavior of the scattered field starting from the spectral solution (2.4), with the eigenvalues and eigenmodes approximated by their slender-body approximations. As in Sec. VI, we only include longitudinal modes in this calculation. For generality, we consider a system of N rings.

Consider first the far-field behavior of the eigenpotentials $\varphi^{(l)}(\mathbf{x})$, whose slender-body approximations are

[cf. (4.3)]

$$\varphi^{(l)}(\mathbf{x}) = \sum_{n=1}^N \frac{a_n}{4\pi\epsilon_0} \int_0^{2\pi} d\phi' \frac{q_n^{(l)}(\phi')}{|\mathbf{x} - \mathbf{y}_n(\phi')|}. \quad (\text{D1})$$

Using the asymptotic behavior

$$\frac{1}{|\mathbf{x} - \mathbf{y}_n|} \sim \frac{1}{|\mathbf{x}|} + \frac{\mathbf{x} \cdot \mathbf{y}_n}{|\mathbf{x}|^3} \quad \text{as } |\mathbf{x}| \rightarrow \infty, \quad (\text{D2})$$

for $n = 1, 2, \dots, N$, and the zero-charge constraints $\int_0^{2\pi} d\phi q_n^{(Z)} = 0$, (D1) gives

$$\varphi^{(Z)}(\mathbf{x}) \sim \frac{\mathbf{x}}{4\pi\epsilon_0|\mathbf{x}|^3} \cdot \sum_{n=1}^N a_n \int_0^{2\pi} d\phi \mathbf{y}_n q_n^{(Z)} \quad \text{as } |\mathbf{x}| \rightarrow \infty. \quad (\text{D3})$$

We next note that, for the sake of evaluating the overlap and normalization integrals in (2.4), we may approximate the eigenfield inside the n th ring as

$$\nabla\varphi_n^{(Z)} = \frac{1}{a_n^2} \frac{dv_n^{(Z)}}{d\phi} \frac{\partial \mathbf{y}_n}{\partial \phi}. \quad (\text{D4})$$

Thus, using integration by parts together with the effective Gauss law (4.2), we find

$$\frac{\int dV \mathbf{E}_\infty \cdot \nabla\varphi^{(I)}}{\int dV \nabla\varphi^{(I)} \cdot \nabla\varphi^{(I)}} = \frac{\sum_{n=1}^N a_n \int_0^{2\pi} d\phi \mathbf{E}_\infty \cdot \mathbf{y}_n q_n^{(I)}}{\sum_{n=1}^N a_n \int_0^{2\pi} d\phi v_n^{(I)} q_n^{(I)}}. \quad (\text{D5})$$

We emphasize that this result is valid even for azimuthally nonuniform rings and arbitrary cross-sectional shapes.

With the above slender-body approximations, the spectral solution (2.4) gives the far-field behavior (6.1), with the polarization tensor α given by (6.3).

-
- [1] S. A. Maier, *Plasmonics: Fundamentals and Applications* (Springer, New York, 2007).
- [2] V. V. Klimov, *Nanoplasmonics* (CRC Press, Boca Raton, FL, 2014).
- [3] I. Romero, J. Aizpurua, G. W. Bryant, and F. J. García De Abajo, *Opt. Express* **14**, 9988 (2006).
- [4] J. A. Schuller, E. S. Barnard, W. Cai, Y. C. Jun, J. S. White, and M. L. Brongersma, *Nat. Mater.* **9**, 193 (2010).
- [5] J. Y. Suh, C. H. Kim, W. Zhou, M. D. Huntington, D. T. Co, M. R. Wasielewski, and T. W. Odom, *Nano Lett.* **12**, 5769 (2012).
- [6] H. Chen, L. Shao, Q. Li, and J. Wang, *Chem. Soc. Rev.* **42**, 2679 (2013).
- [7] G. Toscano, S. Raza, W. Yan, C. Jeppesen, S. Xiao, M. Wubs, A. P. Jauho, S. I. Bozhevolnyi, and N. A. Mortensen, *Nanophotonics* **2**, 161 (2013).
- [8] H. Tamaru, H. Kuwata, H. T. Miyazaki, and K. Miyano, *Appl. Phys. Lett.* **80**, 1826 (2002).
- [9] L. Gunnarsson, T. Rindzevicius, J. Prikulis, B. Kasemo, M. Käll, S. Zou, and G. C. Schatz, *J. Phys. Chem. B* **109**, 1079 (2005).
- [10] P. K. Jain, W. Huang, and M. A. El-Sayed, *Nano Lett.* **7**, 2080 (2007).
- [11] V. V. Klimov and D. V. Guzatov, *Phys. Rev. B* **75**, 024303 (2007).
- [12] A. Aubry, D. Y. Lei, S. A. Maier, and J. B. Pendry, *Phys. Rev. Lett.* **105**, 233901 (2010).
- [13] A. Aubry, D. Y. Lei, S. A. Maier, and J. B. Pendry, *ACS Nano* **5**, 3293 (2011).
- [14] V. V. Lebedev, S. S. Vergeles, and P. E. Vorobev, *Appl. Phys. B* **111**, 577 (2013).
- [15] J. B. Pendry, A. I. Fernández-Domínguez, Y. Luo, and R. Zhao, *Nat. Phys.* **9**, 518 (2013).
- [16] S. Kadkhodazadeh, J. R. de Lasson, M. Beleggia, H. Kneipp, J. B. Wagner, and K. Kneipp, *J. Phys. Chem. C* **118**, 5478 (2014).
- [17] O. Schnitzer, *Phys. Rev. B* **92**, 235428 (2015).
- [18] O. Schnitzer, V. Giannini, R. V. Craster, and S. A. Maier, *Phys. Rev. B* **93**, 041409(R) (2016).
- [19] O. Schnitzer, V. Giannini, S. A. Maier, and R. V. Craster, *Proc. R. Soc. A* **472**, 20160258 (2016).
- [20] O. Schnitzer, *Eur. J. Appl. Math* **31**, 246 (2020).
- [21] S. Yu and H. Ammari, *SIAM Rev.* **60**, 356 (2018).
- [22] S. Yu and H. Ammari, *Proc. Natl. Acad. Sci. USA* **116**, 13785 (2019).
- [23] S. Link and M. A. El-Sayed, *J. Phys. Chem. B* **103**, 8410 (1999).
- [24] C. Sönnichsen, T. Franzl, T. Wilk, G. von Plessen, J. Feldmann, O. V. Wilson, and P. Mulvaney, *Phys. Rev. Lett.* **88**, 077402 (2002).
- [25] S. Prescott and P. Mulvaney, *J. Appl. Phys.* **99**, 123504 (2006).
- [26] B. N. Khlebtsov and N. G. Khlebtsov, *J. Phys. Chem. C* **111**, 11516 (2007).
- [27] F. Neubrech, A. Pucci, T. W. Cornelius, S. Karim, A. García-Etxarri, and J. Aizpurua, *Phys. Rev. Lett.* **101**, 157403 (2008).
- [28] G. Lu, T. Zhang, W. Li, L. Hou, J. Liu, and Q. Gong, *J. Phys. Chem. C* **115**, 15822 (2011).
- [29] Y. O. Agha, O. Demichel, C. Girard, A. Bouhelier, and G. C. des Francs, *Prog. Electromagn. Res.* **146**, 77 (2014).
- [30] Y. Deng, H. Liu, and G. Zheng, *J. Math. Pure Appl.* **153**, 248 (2021).
- [31] A. Moussiaux, A. Ronveaux, and A. Lucas, *Can. J. Phys.* **55**, 1423 (1977).
- [32] J. Aizpurua, P. Hanarp, D. S. Sutherland, M. Käll, G. W. Bryant, and F. J. García de Abajo, *Phys. Rev. Lett.* **90**, 057401 (2003).
- [33] A. Mary, A. Dereux, and T. L. Ferrell, *Phys. Rev. B* **72**, 155426 (2005).
- [34] C. M. Dutta, T. A. Ali, D. W. Brandl, T.-H. Park, and P. Nordlander, *J. Chem. Phys.* **129**, 084706 (2008).
- [35] C. F. Bohren and D. R. Huffman, *Absorption and Scattering of Light by Small Particles* (Wiley, Hoboken, NJ, 2008).
- [36] R. C. Voicu and T. Sandu, *Proc. R. Soc. A* **473**, 20160796 (2017).
- [37] C. A. Downing and G. Weick, *Proc. R. Soc. A* **476**, 20200530 (2020).
- [38] E. J. Hinch, *Perturbation Methods* (Cambridge University Press, Cambridge, 1991).
- [39] M. Ruiz and O. Schnitzer, *Proc. R. Soc. A* **475**, 20190294 (2019).
- [40] I. D. Mayergoyz, D. R. Fredkin, and Z. Zhang, *Phys. Rev. B* **72**, 155412 (2005).
- [41] D. Grieser, *Rev. Math. Phys.* **26**, 1450005 (2014).
- [42] T. J. Davis and D. E. Gómez, *Rev. Mod. Phys.* **89**, 011003 (2017).
- [43] J. P. K. Tillett, *J. Fluid Mech.* **44**, 401 (1970).
- [44] G. Batchelor, *J. Fluid Mech.* **44**, 419 (1970).
- [45] R. G. Cox, *J. Fluid Mech.* **44**, 791 (1970).

- [46] J. B. Keller and S. I. Rubinow, *J. Fluid Mech.* **75**, 705 (1976).
- [47] M. D. Van Dyke, *Perturbation Methods in Fluid Dynamics* (Parabolic Press, Stanford, CA, 1975).
- [48] R. A. Handelsman and J. B. Keller, *J. Fluid Mech.* **28**, 131 (1967).
- [49] P. Nordlander, *ACS Nano* **3**, 488 (2009).
- [50] T. H. Chow, Y. Lai, W. Lu, N. Li, and J. Wang, *ACS Mater. Lett.* **2**, 744 (2020).
- [51] A. Gen, J. Patarroyo, J. Sancho-Parramon, N. G. Bastús, V. Puentes, and J. Arbiol, *Nanophotonics* **6**, 193 (2017).
- [52] V. E. Bochenkov, G. Klös, and D. S. Sutherland, *Opt. Mater. Express* **7**, 3715 (2017).
- [53] X. Zong, L. Li, and Y. Liu, *Opt. Mater. Express* **9**, 870 (2019).
- [54] L. Zhang, Z. Dong, Y. M. Wang, Y. J. Liu, S. Zhang, J. K. W. Yang, and C.-W. Qiu, *Nanoscale* **7**, 12018 (2015).
- [55] A. Pattanayak, S. Roy, G. Rana, S. P. Duttagupta, V. G. Achanta, and S. S. Prabhu, *Sci. Rep.* **7**, 16961 (2017).
- [56] M. Zhang, Q. Lu, and B. Ge, *J. Opt.* **48**, 505 (2019).
- [57] B. D. Dana, A. N. Koya, X. Song, and J. Lin, *Plasmonics* **16**, 1557 (2020).
- [58] P. B. Johnson and R. W. Christy, *Phys. Rev. B* **6**, 4370 (1972).
- [59] K. Ando and H. Kang, *J. Math. Anal. Appl.* **435**, 162 (2016).
- [60] D. J. Bergman, *Phys. Rev. B* **19**, 2359 (1979).
- [61] H. Ammari, B. Fitzpatrick, H. Kang, M. Ruiz, S. Yu, and H. Zhang, *Mathematical and Computational Methods in Photonics and Phononics*, Mathematical Surveys and Monographs (American Mathematical Society, Providence, RI, 2018), Vol. 235.
- [62] A.-K. Tornberg and M. J. Shelley, *J. Comput. Phys.* **196**, 8 (2004).
- [63] O. Schnitzer and R. V. Craster, *SIAM J. Appl. Math.* **77**, 2119 (2017).
- [64] F. Paquin-Lefebvre, S. Iyaniwura, and M. J. Ward, *Eur. J. Appl. Math.*, 1 (2020).
- [65] F. Hao, E. M. Larsson, T. A. Ali, D. S. Sutherland, and P. Nordlander, *Chem. Phys. Lett.* **458**, 262 (2008).
- [66] S. R. Pockock, X. Xiao, P. A. Huidobro, and V. Giannini, *ACS Photon.* **5**, 2271 (2018).
- [67] J. D. Jackson, *Classical Electrodynamics* (Wiley, Hoboken, NJ, 2007).
- [68] A. Mary, D. M. Koller, A. Hohenau, J. R. Krenn, A. Bouhelier, and A. Dereux, *Phys. Rev. B* **76**, 245422 (2007).
- [69] A. Aubry, D. Y. Lei, S. A. Maier, and J. B. Pendry, *Phys. Rev. B* **82**, 205109 (2010).
- [70] Z. Ruan and S. Fan, *Phys. Rev. Lett.* **105**, 013901 (2010).
- [71] U. Hohenester and A. Trügler, *Comput. Phys. Commun.* **183**, 370 (2012).
- [72] S. Link, M. B. Mohamed, and M. A. El-Sayed, *J. Phys. Chem. B* **103**, 3073 (1999).
- [73] C. J. Murphy, T. K. Sau, A. M. Gole, C. J. Orendorff, J. Gao, L. Gou, S. E. Hunyadi, and T. Li, *J. Phys. Chem. B* **109**, 13857 (2005).
- [74] D. J. Bergman and D. Stroud, *Phys. Rev. B* **22**, 3527 (1980).
- [75] M. S. Agranovich, B. Z. Katsenelenbaum, A. N. Sivov, and N. N. Voitovich, *Generalized Method of Eigenoscillations in Diffraction Theory* (Wiley-VCH, Weinheim, 1999).
- [76] A. Farhi and D. J. Bergman, in *Plasmonics: Metallic Nanostructures and Their Optical Properties XIII* (SPIE, Bellingham, WA, 2015), Vol. 9547.
- [77] P. Y. Chen, D. J. Bergman, and Y. Sivan, *Phys. Rev. Appl.* **11**, 044018 (2019).
- [78] A. Wokaun, J. P. Gordon, and P. F. Liao, *Phys. Rev. Lett.* **48**, 957 (1982).
- [79] B. T. Draine and P. J. Flatau, *J. Opt. Soc. Am. A* **11**, 1491 (1994).
- [80] R. Carminati, J.-J. Greffet, C. Henkel, and J.-M. Vigoureux, *Opt. Commun.* **261**, 368 (2006).
- [81] D. J. Bergman, P. Y. Chen, and A. Farhi, *Phys. Rev. A* **102**, 063508 (2020).
- [82] C. Sauvan, J.-P. Hugonin, I. S. Maksymov, and P. Lalanne, *Phys. Rev. Lett.* **110**, 237401 (2013).